Crustal seismic imaging from multifold ocean bottom seismometer data by frequency domain full waveform tomography: Application to the eastern Nankai trough

Stéphane Operto, J. Virieux, J.-X. Dessa, G. Pascal

Crustal seismic imaging from multifold ocean bottom seismometer data by frequency domain full waveform tomography: Application to the eastern Nankai trough

S. Operto,[1] J. Virieux,[2] J.-X. Dessa,[1] and G. Pascal[3,4]

Received 13 May 2005; revised 25 April 2006; accepted 25 May 2006; published 19 September 2006.

[1] In offshore surveys, the deep crust is generally investigated by traveltime tomography applied to sparse ocean bottom seismometer data. The inferred velocity models are of limited resolution precluding a quantitative analysis of deep tectonic discontinuities. If dense arrays of ocean bottom seismometers can be deployed, the resulting data sets become amenable to full waveform processing, which should lead to a significant improvement in the resolution of structures. Such acquisition and processing were achieved on the eastern Nankai subduction zone. Full waveform inversion is entirely implemented in the frequency domain, enabling efficient finite difference wave modeling and allowing to limit the inversion to a few discrete frequencies of increasing value. Such a hierarchical procedure defines a multiresolution approach to seismic imaging. The data set was recorded by 93 instruments deployed along a 105-km-long profile. Thirteen frequencies ranging from 3 to 15 Hz were inverted sequentially. Wavelengths imaged by the full waveform inversion typically range between 0.5 and 8 km. Full waveform tomography reveals an intense compression in the upper prism and underlying backstop, as evidenced by several thrusts, the frontal ones still active, corresponding to negative velocity anomalies. The subducting Paleo-Zenisu ridge is also reconstructed, above which stands the décollement. Velocities in the upper mantle beneath the ridge are rather low (7.5 km s^{-1}), suggesting partially serpentinized mantle beneath the ridge. This paper demonstrates the feasibility of full waveform tomography based on dense ocean bottom seismometer data sets and its ability to quantitatively image the entire crust with a significantly improved resolution compared to what is usually achieved through traveltime tomography.

Citation: Operto, S., J. Virieux, J.-X. Dessa, and G. Pascal (2006), Crustal seismic imaging from multifold ocean bottom seismometer data by frequency domain full waveform tomography: Application to the eastern Nankai trough, *J. Geophys. Res.*, *111*, B09306, doi:10.1029/2005JB003835.

1. Introduction

[2] Crustal-scale seismic surveying at sea is most of the time carried out in two dimensions with an array of ocean bottom seismometers (OBS). Instruments are deployed in lines along which shots are fired. The length of the OBS profiles is defined so as to have sufficiently large source-receiver offsets to record turning waves whose refraction depth cover the zone of interest (the Moho, for example).

[3] For standard crustal surveying with large OBS spacings, the data are conventionally exploited through traveltime tomography. The most basic approach only uses first-arrival refraction traveltimes to derive a large-scale velocity model [e.g., *Toomey et al.*, 1994; *Zelt and Barton*, 1998]. The geometry of the main discontinuities can be inferred by combining refracted first arrivals and wide-angle reflections in the tomography [e.g., *Zelt and Smith*, 1992; *Korenaga et al.*, 2000; *Hobro et al.*, 2003]. However, highly heterogeneous structures may prevent the correlation of reflected phases from one OBS gather to the next one, specially when the OBS spacing is large. Without such correlation, the strong geological assumption of a layered velocity model is necessary to tentatively identify and pick phases. Expertise and extrapolation are needed to provide a qualitative interpretation of these coarse seismic profiles.

[4] The number of available instruments that can be deployed during a seismic experiment has recently dramatically increased from typically less than 10 to several tens of OBSs. Designing a multifold crustal-scale OBS experiment with a receiver spacing of 1–2 km while keeping sufficiently long profiles for imaging the lower crust is now possible. However, the receiver spacing remains significantly

[1] Géosciences Azur, Centre National de la Recherche Scientifique-Insitut de Recherche pour le Développement-Université Nice Sophia Antipolis-Université Pierre and Marie Curie, Villefranche-sur-mer, France.
[2] Géosciences Azur, Centre National de la Recherche Scientifique-Insitut de Recherche pour le Développement-Université Nice Sophia Antipolis-Université Pierre and Marie Curie, Valbonne, France.
[3] Ecole Normale Supérieure, Paris, France.
[4] Deceased 15 December 2004.

0148-0227/06/2005JB003835$09.00

larger than the air gun shot spacing (50–200 m) and the seismic coverage of the medium, albeit strongly improved, is still weaker than that currently achieved in multichannel seismics. This new type of multifold wide-aperture data sets is suitable for waveform processings such as prestack depth migration which is the method of choice for multichannel seismic reflection data. However, in the wide-angle geometry, the full wavefield must be taken into account, including refracted, precritical and postcritical reflected waves; this introduces significant differences. In the following, we will define by full waveform tomography (FWT) any quantitative processing that is able to fit waveforms recorded over a broad range of apertures. Considering the whole wavefield is expected to provide a significant improvement in the resolution of tomographic models.

[5] Full waveform inversion was introduced by *Tarantola* [1984] and *Lailly* [1984] in the processing of seismic reflection data. The approach relies on linearized inverse theory [e.g., *Tarantola*, 1987] based on adjoint operators. A misfit norm is defined between observed seismograms and some computed in an initial medium. The optimization iteratively updates the model by minimizing this misfit. Waves are recomputed in the updated model and the procedure is repeated until the misfit function reduction is no more significant. Such linearized optimization will perform successfully if the starting model is close enough to reality. For wide-aperture data, the long-wavelength model can be reconstructed through first-arrival traveltime tomography (FATT). This model should be accurate enough to proceed with linearized FWT [*Pratt*, 1999].

[6] In the optimization procedure, the kernel for modeling the full wave field in heterogeneous media is critical. Among different methods, finite difference (FD) techniques provide a good compromise between accuracy, computational cost, simplicity of implementation and the ability to describe heterogenous models.

[7] Successful applications of FWT to real data remained rare until recently because of the computational cost of the forward problem (multisource full wavefield modeling) and the sensitivity of the method to different sources of error (ground-receiver coupling, source calibration, noise, accuracy of the starting model). More fundamentally, the method was mainly applied to multichannel seismic reflection data, [e.g., *Crase et al.*, 1990, 1992]. In this context, building an initial model of sufficient accuracy has always been a bottleneck since the reflection acquisition geometry is not suited to reconstruct the long wavelengths of a structure.

[8] Two-dimensional FWT based on FD wave modeling was originally developed in the time-space domain [e.g., *Tarantola*, 1984; *Gauthier et al.*, 1986; *Crase et al.*, 1990, 1992; *Pica et al.*, 1990; *Shipp and Singh*, 2002]. The overall computational effort is huge because the FD forward modeling must be fully completed twice per shot: once for a source position corresponding to the shot (forward problem) and once for a fictitious source consisting of a simultaneous excitation of data residuals at receiver positions, as we shall see for the inverse problem. On the other hand, the time domain makes it easier to time window seismic arrivals [*Kolb et al.*, 1986].

[9] To circumvent the limitations of time domain methods, *Pratt and Worthington* [1990] and *Pratt et al.* [1998] developed two-dimensional (2-D) full waveform modeling and tomography in the frequency domain for which the FD modeling of waves is very well adapted to multisource problems like in modern seismic acquisitions [*Pratt and Worthington*, 1990; *Stekl and Pratt*, 1998]. Moreover, attenuation can be easily implemented in frequency domain modeling algorithms using complex velocities. The inverse problem is also solved in the frequency domain by successively inverting one or several discrete frequencies, thus allowing a compact volume of data to be managed [*Pratt et al.*, 1998]. The inversion classically proceeds from low to higher frequencies to inject increasing wave numbers in the tomographic model. This multiscale approach helps to mitigate the nonlinearity of the inverse problem [*Pratt et al.*, 1996]. Moreover, wide-aperture acquisition geometries lead to a strong redundancy in the wave number domain [*Pratt and Worthington*, 1990], as a result of the combined influence of the source frequency and the diffraction angles on the intrinsic resolution of FWT. This redundancy allows decimation of data sets by inverting a selected subset of frequencies (see *Sirgue and Pratt* [2004] for a criterion to define an optimal frequency interval). This is another key point which, in addition to the efficiency of frequency domain wave modeling, makes 2-D frequency domain FWT significantly less computationally intensive than its time domain counterpart.

[10] The dramatic increase in achievable spatial resolution when using waveform tomography in addition to traveltime tomography for crustal experiments was already presented by *Pratt et al.* [1996] for synthetic data. This paper is devoted to the first application of frequency domain FWT to a real crustal-scale OBS data set. The target zone is the highly heterogeneous crustal structure of the eastern Nankai subduction zone (Tokai area). Results of FATT and asymptotic prestack depth migration were already presented by *Dessa et al.* [2004a]. Some preliminary results of FWT applied to this data set were also presented by *Dessa et al.* [2004b]. A smaller-scale application of frequency domain FWT to wide-aperture, on-land seismic data collected in a complex thrust belt in the southern Apennines (Italy) was also performed [*Ravaut et al.*, 2004; *Operto et al.*, 2004].

[11] The second part of the paper reviews the main theoretical principles of frequency domain FWT. Emphasis is then put on the numerical strategies that were specifically developed for acoustic FWT applied to a large OBS data set. We also present a theoretical sensitivity analysis of FWT with respect to FATT. In the third part, the results of FWT on the Nankai multifold OBS data set are shown. The main geological features of the velocity models are described and discussed based on several illustrations (traveltime and waveform modeling) of the data fit. The actual resolution of the FWT images is compared with theoretical predictions. The different sources of error affecting the velocity model are also discussed.

2. Method: Frequency Domain Full Waveform Tomography

[12] The theory of frequency domain FD waveform modeling was described in detail by *Jo et al.* [1996], *Stekl and Pratt* [1998], and *Hustedt et al.* [2004]. Frequency domain FWT was fully described by *Pratt et al.* [1998]. The main issues of this approach are presented here and

some numerical aspects that are specific to OBS applications are clarified.

2.1. Finite Difference Waveform Modeling

[13] The 2-D viscoacoustic wave equation is written in the frequency domain as

$$\frac{\omega^2}{\kappa(x,z)}p(x,z,\omega)+\frac{\partial}{\partial x}\left(\frac{1}{\rho(x,z)}\frac{\partial p(x,z,\omega)}{\partial x}\right)+\frac{\partial}{\partial z}\cdot\left(\frac{1}{\rho(x,z)}\frac{\partial p(x,z,\omega)}{\partial z}\right)=-s(x,z,\omega) \quad (1)$$

where $\rho(x, z)$ is the density, $\kappa(x, z)$ the complex bulk modulus, ω the frequency, $p(x, z, \omega)$ the pressure field and $s(x, z, \omega)$ is the source. Attenuation effects can be easily implemented thanks to complex P wave velocities in the expression of the bulk modulus [*Töksoz and Johnston*, 1981].

[14] Since the relationship between the pressure wavefield and the source is linear, the viscoacoustic wave equation (1), can be recast in a matrix form as

$$\mathbf{Ap}=\mathbf{s} \quad (2)$$

where the complex-valued impedance matrix **A** depends on the frequency and medium properties. The 2-D pressure **p** and source **s** fields at one frequency ω are stored as vectors of dimension $nx \times nz$ where nx and nz are the dimensions of the regular FD grid, with a grid interval h. The pressure field is obtained by solving the system of linear equations. If a direct method can be used to solve (2), solutions for multiple sources (i.e., multiple right-hand side terms) can be efficiently obtained by forward and backward substitutions once the matrix **A** is factorized using a LU decomposition scheme for instance: The wave equation (1) is discretized in a FD sense using the so-called mixed-grid approach [*Jo et al.*, 1996; *Stekl and Pratt*, 1998; *Hustedt et al.*, 2004]. *Hustedt et al.* [2004] provide further details about the FD algorithm used here. The solution of (2) was computed through a distributed-memory parallel multifrontal scheme developed by *Amestoy et al.* [2000, 2001].

[15] Although marine seismic experiments are carried out with explosive sources, we will see that both explosions and vertical forces need to be implemented in the frequency domain FD wave propagation code to mimic an acoustic source whose signal is recorded by vertical geophones.

2.2. Frequency Domain Full Waveform Inversion

[16] The weighted least squares linearized waveform inversion is solved in the frequency domain by a classic gradient method [*Pratt et al.*, 1998]. The weighted least squares norm of the cost function is given by

$$\mathcal{C}(\mathbf{m})=\Delta\mathbf{d}^{\dagger}\mathbf{W}_d\Delta\mathbf{d} \quad (3)$$

where $\Delta\mathbf{d}$ is the vector of residuals (the difference between the observed data and those computed in model **m**). The superscript † indicates the adjoint, i.e., the transpose conjugate. $\mathbf{W}_d$ is a weighting operator applied to the data in order to scale the relative contribution of each component of the vector $\Delta\mathbf{d}$ in the inversion.

[17] In its standard form, the gradient method provides the following relation between model perturbations and the weighted data residuals

$$\Delta\mathbf{m}=-\alpha\nabla_{\mathbf{m}}\mathcal{C}=-\alpha Re\{\mathbf{J}^t\mathbf{W}_d\Delta\mathbf{d}^*\} \quad (4)$$

where $\Delta\mathbf{m}$ is the model perturbation (the updated model **m** is related to the starting model $\mathbf{m}_0$ by $\mathbf{m}=\mathbf{m}_0+\Delta\mathbf{m}$), $\nabla_{\mathbf{m}}C$ is the gradient of the cost function, α is a step length which controls the amplitudes of the perturbations, $\mathbf{J}^t$ is the transpose of the Jacobian matrix (i.e., the Fréchet derivative matrix), $\Delta\mathbf{d}^*$ is the conjugate of data residuals and *Re* denotes the real part of a complex number.

[18] The Jacobian matrix **J** is given by

$$\mathbf{J}=-\mathbf{A}^{-1}\frac{\partial\mathbf{A}}{\partial\mathbf{m}}\mathbf{p} \quad (5)$$

where **p** denotes the forward modeled pressure wavefields [*Pratt et al.*, 1998, equations (15) and (16)]. The columns of the matrix $\mathbf{A}^{-1}$ are the green functions for sources located at each grid node of the velocity model. Inserting the expression of the Jacobian matrix **J** (5), in (4), and exploiting the source-receiver reciprocity principle, $\mathbf{A}^{-1}=\mathbf{A}^{-1^t}$, give for the ith model perturbation

$$\Delta m_i=\alpha Re\left\{\mathbf{p}^t\left[\frac{\partial\mathbf{A}^t}{\partial m_i}\right]\mathbf{A}^{-1}\mathbf{W}_d\Delta\mathbf{d}^*\right\} \quad (6)$$

[19] Equation (6) indicates that the gradient is formed by a zero-lag convolution of the modeled wavefield **p** with the backward propagated weighted residuals $\mathbf{A}^{-1}\mathbf{W}_d\,\Delta\mathbf{d}^*$. We easily compute the matrix $\partial\mathbf{A}^t/\partial m_i$ from the coefficients of **A**. This matrix is extremely sparse since it represents an operator of local support centered around the position of parameter i. Equation (6) requires the computation of only two forward modeling problems (i.e., forward and backward substitutions) per shot position: the first forward problem computes the wavefield **p** for a source located at the shot position. The second one computes the backward propagated residual wavefield $\mathbf{A}^{-1}\Delta\mathbf{d}^*$ using a "composite" source formed by assembling the data residuals. We avoid the explicit computation of the Jacobian matrix.

[20] In order to obtain reliable perturbation models, we applied some scalings and regularizations to the gradient (6). The inversion formula used in this study is given by

$$\Delta\mathbf{m}=-\alpha(diag\mathbf{H}_a+\epsilon I)^{-1}\mathcal{G}_{\mathbf{m}}Re\left\{\mathbf{p}^t\left[\frac{\partial\mathbf{A}^t}{\partial m_i}\right]\mathbf{A}^{-1}\mathbf{W}_d\Delta\mathbf{d}^*\right\} \quad (7)$$

where $diag\ \mathbf{H_a} = diag\ Re\ \{\mathbf{J}^t\ \mathbf{W}_d\ \mathbf{J}^*\}$ denotes the diagonal elements of the weighted approximate Hessian $\mathbf{H_a}$ and $\mathcal{G}_{\mathbf{m}}$ is a spatial smoothing operator.

[21] The diagonal of the approximate Hessian provides a preconditioner of the gradient that properly scales the perturbation model [*Shin et al.*, 2001]. An example of this gradient preconditioning was shown by *Ravaut et al.* [2004, Figure 12] in the case of a land refraction experiment. These diagonal terms correspond to the autocorrelation of the partial derivative wavefields, or in other words, to the squared product of the source and receiver Green functions

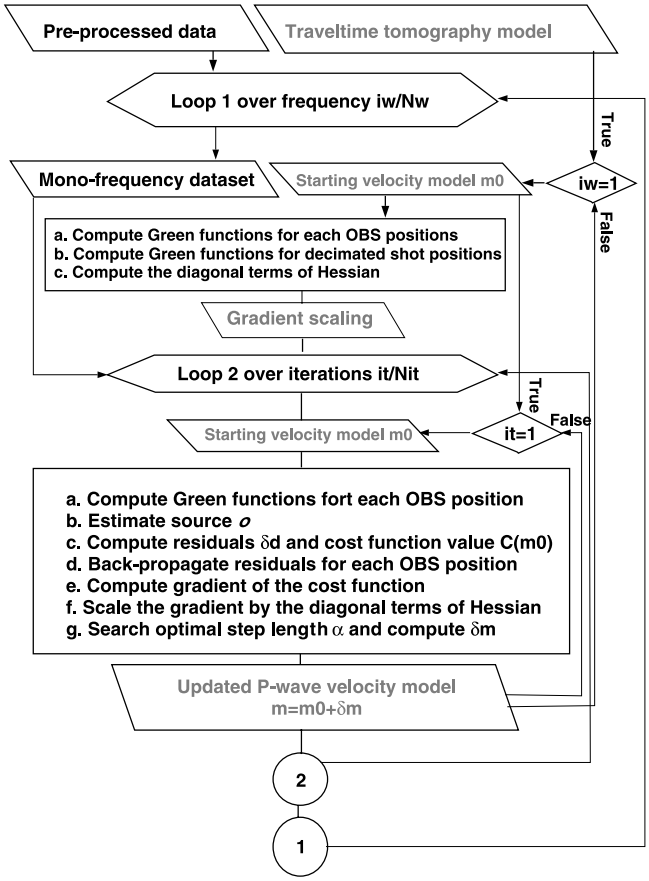

Figure 1. Flowchart of the frequency domain FWT applied to OBS data for which $N_s \gg N_r$. The grey text indicates processing outputs.

[*Pratt et al.*, 1998]. Dividing the data residuals by these squared amplitude terms is equivalent to removing the effect of the geometrical amplitude decay of the source and receiver Green functions from the data residuals. For a surface acquisition geometry, this gradient preconditioning helps to properly scale the deep perturbations constrained by long-offset/small-amplitude traces with respect to the shallow perturbations constrained by short-offset/large-amplitude ones. We fixed velocities within the first one hundred meters below the sea bottom during the inversion to avoid model perturbations near the receiver positions where a suitable scaling of the gradient is difficult to perform.

[22] The smoothing operator $\mathcal{G}_{\mathbf{m}}$ is a 2-D Gaussian spatial filter whose correlation lengths are adapted to the inverted frequency [*Ravaut et al.*, 2004]. We tuned this smoothing so that the resolution of the velocity models roughly matches that predicted by the sensitivity kernel of FWT.

[23] The operator $\mathbf{W}_d$ is an amplitude gain with offset applied to each seismic trace:

$$W_d(o_{sr}) = \exp(g \log|o_{sr}|) \tag{8}$$

where the scalar g controls the amplitude of the gain with respect to the source-receiver offset o_{sr}. This weighting allows the decrease of the relative contribution of small offsets, which generally carry little information on the deep structure since they are dominated by the direct water wave and diffractions in the sedimentary layers.

[24] The perturbation model $\Delta\mathbf{m}$ is discretized on a decimated version of the FD grid used for the forward problem. Once a perturbation model was computed on the inversion grid, it is linearly interpolated on the forward modeling grid in order to proceed to the next iteration.

2.3. Algorithmic Aspects

2.3.1. Computation of the Diagonal Hessian

[25] Computing the diagonal elements of the approximate Hessian implies the explicit calculation of the Jacobian matrix $\mathbf{J}$ and, hence to compute the Green functions for sources located at each shot and receiver position. Considering a standard refraction experiment for which each receiver records all the shots, the number of forward problems to solve for computing the gradient is $2 \times \min(N_s, N_r)$ where N_s and N_r are the numbers of shots and receivers, respectively. The computation of the Jacobian requires the computation of $N_s + N_r$ forward problems. If the number of shots is significantly greater than the number of receiver positions, $N_s \gg N_r$ as for OBS experiments, this operation is significantly more expensive than the gradient computation. To overcome this difficulty, we computed the Jacobian only once per frequency, before the first iteration, and with a decimated shot acquisition. The same gradient scaling is then applied for all iterations of the inversion at that frequency. At each iteration, the gradient of the cost function is computed using the full acquisition geometry by backpropagating the residuals associated with one shot in one go, leading to $2 \times N_r$ forward/backward substitutions.

[26] The flowchart in Figure 1 summarizes the main steps of our algorithm. The input parameters required by our FWT algorithm were detailed by *Ravaut et al.* [2004] and *Operto et al.* [2004]. In our present procedure, we invert only for P wave velocities although the FD modeling program can handle three classes of parameters: velocity, density and attenuation. The density and attenuation were kept constant and equal to 1 and 10^4, respectively, during waveform inversion.

2.3.2. Fitting Observed Vertical Geophone Data With Pressure Synthetics

[27] The OBS data processed in this paper were recorded with vertical geophones that record vertical particle velocity. The acoustic FD modeling code computes the pressure field. The two wavefields have very contrasted amplitude-versus-offset behaviors since hydrophones are insensitive to the incidence angle of the wave, in contrast with directional sensors such as geophones. In Appendix A, we develop the spatial reciprocity relationship between vertical particle velocity wavefields generated by explosions and pressure wavefields generated by a vertical force. This relationship allowed us to match the OBS data recorded by vertical geophone with pressure synthetics under the acoustic approximation.

[28] The reciprocity relationship has two key implications for the acoustic waveform inversion of OBS data: first, it allows processing of the observed vertical geophones data as pressure by replacing explosive sources with vertical forces in the FD modeling equation (2); second, it allows use of the gradient expression of (6) developed for the single pressure wavefield rather than developing an equiv-

alent for the vertical velocity field. This would have required to manipulate two wavefields, horizontal and vertical velocities, like for the elastic wave equation, instead of one single pressure field.

[29] The exact modeling of the amplitude versus offset behavior of vertical geophone data with pressure synthetic wavefield is new compared to the algorithms used by *Ravaut et al.* [2004], *Operto et al.* [2004], and *Dessa et al.* [2004b] for which an empirical amplitude normalization was applied by whitening the vertical geophone data to mimic the amplitude-versus-offset behavior of pressure wavefield. This trick yields a much improved reduction of the cost function.

2.3.3. Source Estimation

[30] FWT requires the estimation of the source term featuring in the right-hand side of (2) [e.g., *Pratt*, 1999]. We used the same approach as that described by *Ravaut et al.* [2004]. The source term is estimated by solving a linear inverse problem with an associated forward problem

$$\mathbf{A}\,\mathbf{p} = o\,\mathbf{s} \tag{9}$$

where $\mathbf{s}$ is an a priori estimate of the source term and o is a complex-valued scalar to be determined at each inverted frequency. The least squares solution is given by

$$o = \frac{\mathbf{p_0}^t\mathbf{d}^*}{\mathbf{p_0}^t\mathbf{p_0}^*} = \frac{\sum_{i=1}^{N} p_{0i} d_i^*}{\sum_{i=1}^{N} p_{0i} p_{0i}^*} \tag{10}$$

where $\mathbf{d}$ is the data vector and $\mathbf{p_0}$ is the wave field computed for the source estimate $\mathbf{s}$. In (10), the scalar o is computed by summing over the full data set, N denoting the total number of source-receiver pairs. A strong assumption of this approach is that the velocity structure used for that purpose accurately predicts the data if the source is known. For OBS data, the direct water wave should have a dominant contribution in the least squares source estimation because of its high amplitude. Since the water velocity is well known, the above mentioned assumption should be reasonably verified. We did not apply the operator $\mathbf{W_d}$ in (10) in order to favor the short-offset traces where the water wave is dominant. The source estimation is directly implemented in the FWT algorithm, before the estimation of the data residuals rather than prior to the waveform inversion (Figure 1). This somewhat blind source estimation procedure was assessed with a complex onshore synthetic example involving a weathered layer near the surface [*Ravaut et al.*, 2004]. The results suggested that the source estimation allowed absorbtion of some inaccuracies of the subsurface of the starting velocity model. This is achieved in the frequency domain and only for the inverted frequencies. Moreover, one frequency of the source is reestimated at each iteration of the inversion.

2.4. Sensitivity Kernel of Frequency Domain Full Waveform Tomography

[31] The main contribution of FWT compared to FATT is a resolution improvement of the Earth's model. Therefore we need rules for a rough estimation of the intrinsic resolution permitted by this approach and its relationship with the acquisition design. In the following analysis, we assume that shots and receivers are continuously sampled although the OBS spacing is an important factor which limits the FWT resolution. The spacing between OBSs controls the fold of the acquisition, which must be greater than one to avoid spatial aliasing. For a wide-aperture experiment, the fold may be defined as $\mathcal{L}/2\Delta O$ where the OBS spacing and the range of offsets over which a reflection is observed in an OBS gather are denoted by ΔO and $\mathcal{L}$, respectively. Hence it depends on the offset range over which a reflection is really observed. This range in turn may depend on several factors such as the depth of the target, the signal-to-noise ratio, the nature of the reflecting boundary (first-order discontinuity, high-velocity gradient zone) and its lateral continuity. For example, deep reflections are unlikely to be observed at short offsets due to their weak amplitudes at these incidences. This makes the real fold generally much smaller than theory would predict, at least for deep targets. Therefore we find it difficult to draw some definitive rules about the largest OBS spacing allowed designation of a wide-aperture experiment in the prospect of FWT. Here, we limit our analysis on the relationship between the illumination aperture, the source frequency bandwidth and the size of the structures that can be images by FWT.

[32] Assuming a homogeneous medium of velocity c above a reflecting point at a depth z and a frequency f, it can be shown through a high-frequency asymptotic analysis [*Miller et al.*, 1987; *Lambaré et al.*, 2003] that the vertical wave number locally characterized around the point is given by

$$k_z = \frac{2f}{c}\cos\frac{\theta}{2} \tag{11}$$

where the aperture θ is related to the offset o_{sr} and depth z by

$$\tan\frac{\theta}{2} = \frac{o_{sr}}{2z} \tag{12}$$

Equation (11) shows that one temporal frequency and one aperture component of the data span one wave number in the model [*Wu and Töksoz*, 1987; *Devaney*, 1982]. The critical parameter that controls the resolution of seismic imaging, together with frequency, is the aperture and not the offset. If a global aperture configuration is available, i.e., if apertures range from 180° to 0°, one frequency spans a broad range of wavelengths ranging theoretically from the (local) average properties of the medium to half of the minimum wavelength. In other words, inversion of one single frequency of the data is theoretically sufficient to image a low-pass-filtered version of the true Earth structure. Formula (11) also implies that one frequency contains the full information of a lower frequency if a wide-aperture acquisition geometry is available [*Pratt and Worthington*, 1990]. Successive inversions of increasing frequencies allow addition of higher wave numbers to the tomographic image and hence to focus it by broadening its wave number spectrum.

[33] The resolution of FWT can be also assessed in the frequency domain through a wave path analysis (Figure 2). A wave path is an interference picture obtained by multi-

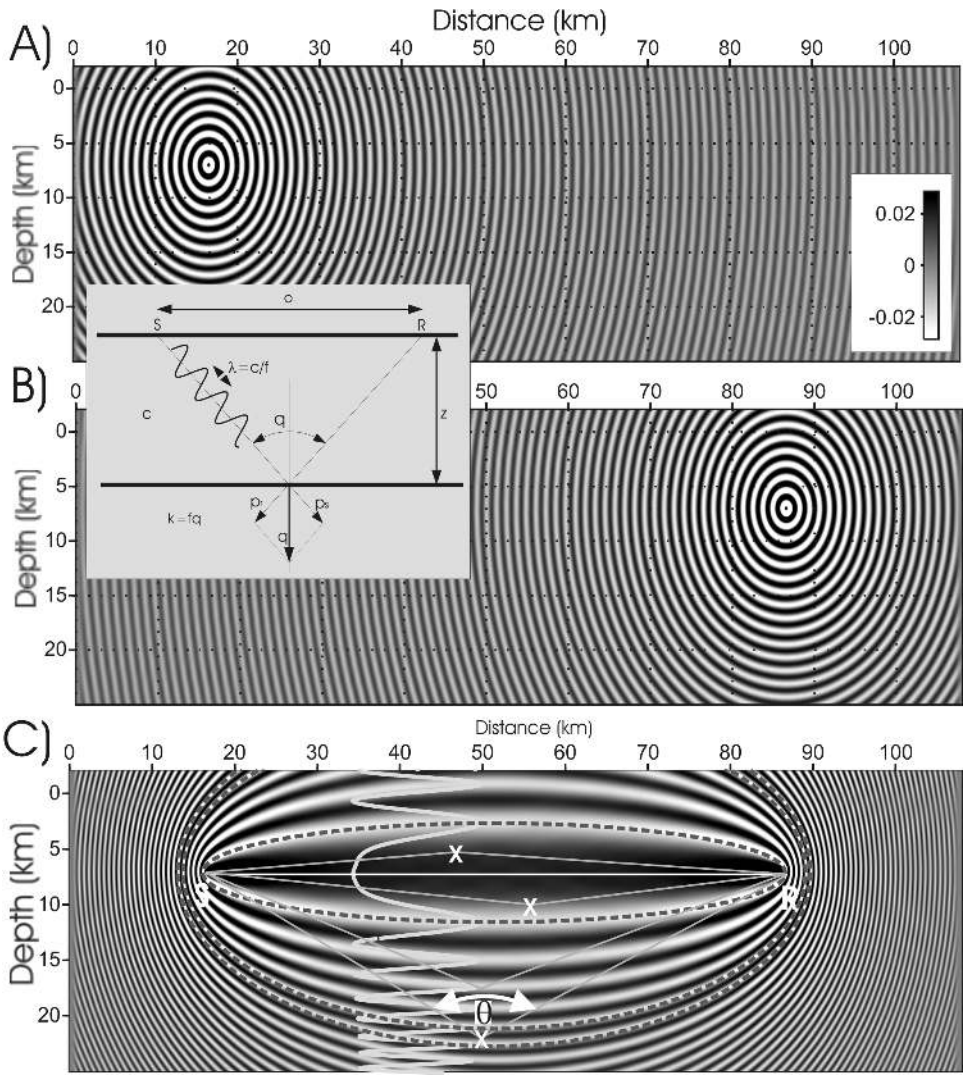

Figure 2. Sensitivity kernel of FWT at crustal scale derived from a wave path analysis. Real part of monochromatic (a) source and (b) receiver Green functions. The frequency is 5 Hz, and the background velocity is homogeneous (6 km s^{-1}). The model dimensions are 110 × 25 km. (c) Real part of the wave path. The dashed lines delineate the first Fresnel zone (central lobe) and one isochrone surface (outer fringe). The minimum traveltime ray path is represented by the straight line connecting the shot to the receiver. Two forward scattered ray paths associated with diffractors lying in the first Fresnel zone as well as two backscattered ray paths with different reflection depths are plotted. The oscillating curve is a vertical section of the wave path. The inset summarizes the representative parameters of a seismic experiment and their relation with spatial resolution of seismic imaging. Nomenclature is o, source-receiver offset; S, source position; R, receiver position; z, depth of interface; c, P wave velocity; f, frequency; λ, propagated wavelength; θ, aperture angle; $\mathbf{p}_s$ and $\mathbf{p}_r$, slowness vectors; $\mathbf{k}$: wave number vector; $\mathbf{q} = \mathbf{p}_s + \mathbf{p}_r$. The vertical wave number $\mathbf{k}$ is related to the slowness vector $\mathbf{q}$ by $\mathbf{k} = f\mathbf{q}$.

plying monochromatic Green functions from a source and a receiver [*Woodward*, 1992]. It is the sensitivity kernel of the Born integral that linearly relates a model of velocity perturbation to the wavefield that is diffracted on it. The nature of the Born wavefield can be easily interpreted from the wave path expression: a single-scattered wavefield is built by summing the traveltimes and multiplying the amplitudes of the Green functions from the source S to a diffractor X and from the diffractor to the receiver R, respectively. In the Born-linearized inverse problem, the wavefield diffracted by the unknown perturbation model corresponds to the data residuals. Waveform inversion projects these residuals back over wave paths. Hence delineation of areas of constant or smoothly varying phase in the wave path provides a clear insight in the resolution that can be achieved through FWT. The major feature of refracted wave paths is a broad area wherein the phase varies very smoothly and whose shape is elliptical in the case of a homogeneous velocity background: It exhibits a banana-shaped pattern in the more realistic case of a positive velocity gradient with depth. This area is centered on the Fermat ray path of minimum traveltime and it

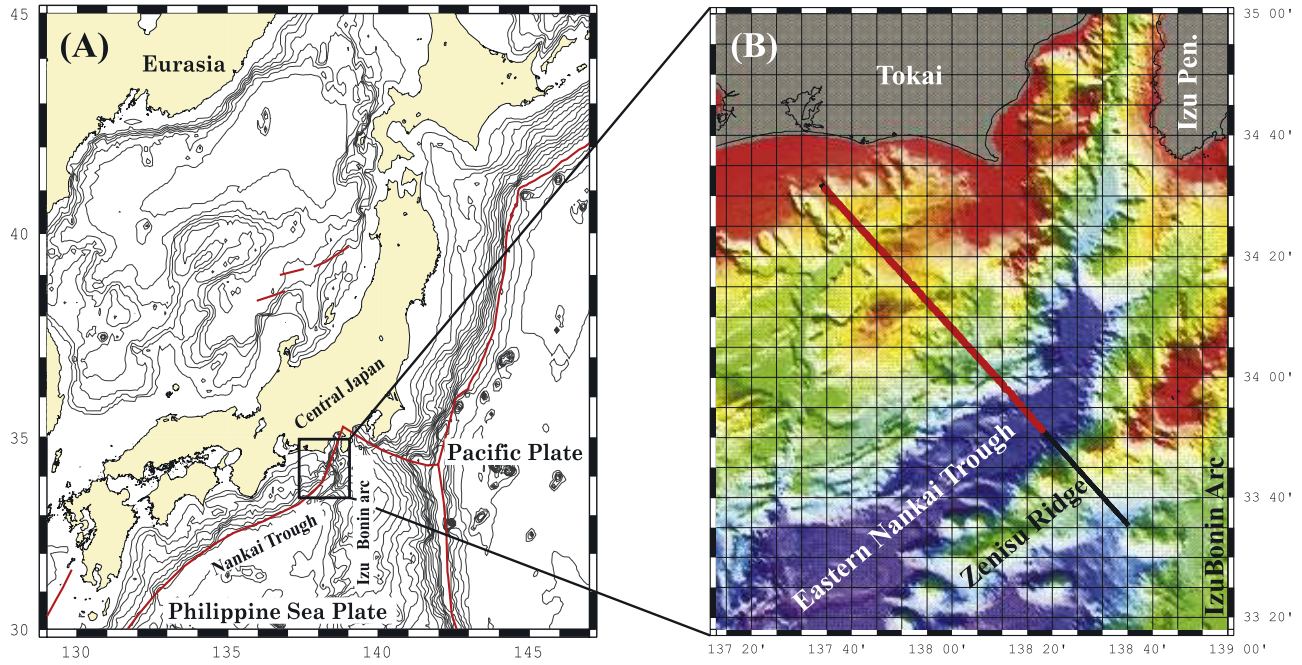

Figure 3. (a) General geodynamic setting around the Nankai trough. (b) Zoom of the box shown in Figure 3a with the main structures of the survey area. The straight black line is the shot profile of concern here. The thicker coincident red line corresponds to the OBS array.

corresponds to the first Fresnel zone [*Woodward*, 1992]: any diffractor X within this zone yields a perturbation wavefield whose arrival delay is less than half a period as compared to the minimum traveltime. Since arrivals are not separable within this range of delays according to the Rayleigh criterion, any diffraction in the first Fresnel zone is a contribution to the first arrival. In the reciprocal reasoning, the first arrival residuals will be projected back onto the first Fresnel zone during waveform inversion, hence providing an image of the large-scale velocity structure whose spatial extent is about $\sqrt{\lambda o_{sr}}$, that is, the width of this zone where λ is wavelength. Surrounding the central lobe, the outer fringes describe some isochrone surfaces that are associated with reflection ray paths ($S - X - R$) of constant travel times. In a migration-like processing, a reflection event recorded with a traveltime T is projected back over the isochrone surface corresponding to that traveltime. The vertical resolution of migration is given by the width of the isochron: $c/2f\cos(\theta/2)$, the inverse of the vertical wave number in (11). The width of isochrone surfaces decreases with depth, i.e., with aperture, illustrating again the relationship between resolution and aperture.

[34] This resolution analysis illustrates that FWT applied to global aperture data embeds a transmission-like and a migration-like waveform processing [*Pratt et al.*, 1996]. While waveform processing continuously proceeds from the large apertures to smaller ones, the tomographic reconstruction evolves from the transmission to the reflection regime. Such gradual transition can be illustrated by the fact that in the time-offset domain, supercritical reflected arrivals from an interface tend asymptotically to the turning wave refracted just above it. This gives an insight as to why these two arrivals of different natures asymptotically carry the same large-scale information on the medium.

[35] The wave path displayed in Figure 2 corresponds to parameters that are representative of a deep crustal experiment. The offset is 70 km, the velocity (uniform here) is 6 km s^{-1}, and the frequency is 5 Hz. This leads to a width of the first Fresnel zone of 9 km. At a depth of 15 km, the aperture angle is 120° and the vertical resolution is 1.2 km for this aperture. Indeed, if higher frequencies and smaller apertures can be exploited, the vertical resolution of deep reflectors imaging will be improved as suggested by (11). Comparison between the width of the first Fresnel zone and the width of the isochron surfaces highlights the dramatic improvement of spatial resolution (one order of magnitude) in the crustal models which can be expected from FWT as compared to FATT.

3. Application to the Eastern Nankai Trough

3.1. The SFJ-OBS Experiment: Target Zone and Experimental Setup

[36] The data presented and processed hereafter were acquired during the KY0106 cruise, performed by the Institute for Frontier Research on Earth Evolution (IFREE) between 29 July and 6 September 2001 on R/V Kaiyo as part of the collaborative French-Japanese Seize France Japan (SFJ) project (Figure 3). The aim of the SFJ-OBS experiment was to perform high-resolution deep crustal imaging of the easternmost segment of the Nankai trough (central Japan).

3.1.1. Eastern Nankai Trough

[37] The Nankai trough marks the boundary along which the Philippine Sea plate subducts beneath the Japanese arc along a N310° direction, with a convergence velocity of ~4.5 cm yr^{-1} [*Seno et al.*, 1993]. This subduction is prone to large megathrust earthquakes that are historically well documented [e.g., *Ando*, 1975b]. Seismic ruptures are

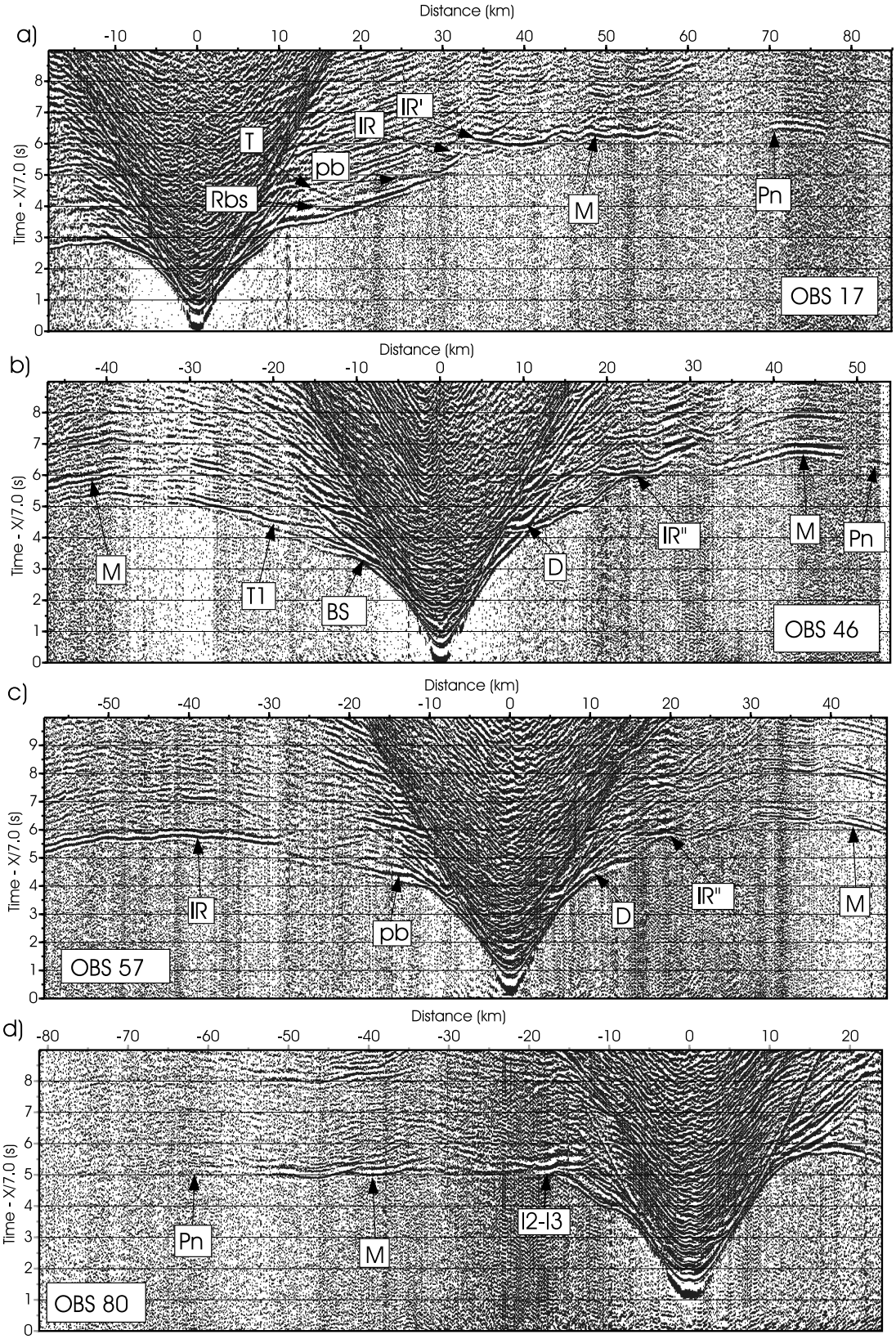

Figure 4. Four examples of OBS gather: (a) OBS 17; (b) OBS 46; (c) OBS 57; (d) OBS 80. The main reflected arrivals are labeled as well as the refraction in the upper mantle (Pn). M is the reflection on the Moho (see text for details).

segmented and there is evidence that some events break a part of the whole subduction thrust (be it one segment or more) whereas some others (in 1707 for instance) would occasionally rupture the whole thrust, i.e., the 4 or 5 five segments that authors classically identify [*Ando*, 1975b; *Kumagai*, 1996; *Cummins et al.*, 2002]. The recurrence intervals of these large ruptures are 100 to 200 years. The last two cycles of ruptures have been the 1854 double event, during which the whole thrust has been ruptured by two earthquakes that triggered within a few hours, and the 1944 and 1946 earthquakes that left the whole system released, except for the easternmost segment [*Ando*, 1975b]. The latter thus remains unruptured since 1854, which has lead authors to consider that a megathrust event along this eastern Nankai-Suruga trough (often referred to as the Tokai segment) is likely to happen in a close future [*Ando*, 1975a; *Le Pichon et al.*, 1996].

[38] An important effort has been undertaken to correlate the segment boundaries with structural discontinuities along the system (see *Dessa et al.* [2004a] and references therein for a review). As for the unruptured Tokai segment, the tectonic setting is significantly different than along the rest of the Nankai subduction due to its immediate proximity with the collision zone of the Izu-Bonin arc with central Japan (Izu collision zone). It therefore exhibits an intermediate behavior between subduction and collision [e.g., *Mazzotti et al.*, 1999], with in particular, an intraoceanic shortening and the formation of trench-parallel compressive ridges that is thought to be cyclical [*Mazzotti et al.*, 2002; *Kodaira et al.*, 2003]. Such a 2- to 3-km-high feature, the Zenisu ridge [*Lallemant et al.*, 1989], is presently close to entering the trench; there is strong evidence of an analogous ridge, the Paleo-Zenisu ridge, beneath the accretionary prism [*Lallemand et al.*, 1992; *Le Pichon et al.*, 1996; *Dessa et al.*, 2004a] and a third deeper ridge subducting beneath the fore arc has even been proposed by *Kodaira et al.* [2003] on tomographic evidence. The existence of these subducting ridges is obviously a strong factor of segmentation for large seismic ruptures along the subduction thrust and it is essential to have some confirmation of their presence and an insight of their interaction with the surrounding structures, particularly regarding the strong deformation regime they must imply in the upper plate and possibly in the underlying oceanic crust.

[39] Bringing answers to these questions requires a deep and sharp imaging of structures for which a global offset seismic experiment is necessary. An acquisition of this type was realized in the frame of the afore mentioned SFJ project.

3.1.2. Experimental Setup

[40] A dense array of 100 OBSs was deployed along a line oriented N 314°, roughly perpendicular to the margin's structures (Figure 3b). The OBSs were 1 km apart, leading to a 100-km-long receiver line. This geometry appears to offer the best compromise between completeness and density of the spatial coverage with respect to the targeted structures. A 140-km-long shot profile, coincident with the OBS line, was acquired with a 100-m spacing between successive shots (1404 shot positions). It was acquired in two boat passes, with staggered source positions, spaced 200 m apart, thanks to the accurate positioning provided by differential global positioning (D-GPS). Data were subsequently merged. This procedure allows the use of a greater delay between successive shots, thus diminishing the noise that possibly results from previous shots [*Nakamura et al.*, 1987].

[41] The seismic source consists of an array of eight 1500 cubic inch air guns, for a total source volume of 196 L. Shot positions were controlled by D-GPS. The OBSs, provided by the Japan Marine Science and Technology (JAMSTEC), are equipped with a three-component geophone (4.5 Hz) and a hydrophone [*Shinohara et al.*, 1993]. Sampling rate was 10 ms, and their positioning was controlled through a supershort base line (SSBL) system, with a depth accuracy of 2–3%. Three of the OBSs were not recovered. Of the others, 93 provided exploitable data. In this study, we only deal with data from the vertical component of geophones rather than those of the hydrophones which appear to be of poorer quality (Figure 4).

[42] Other examples of OBS gathers were presented by *Dessa et al.* [2004a]. Although several refracted and wide-angle reflected phases can be interpreted, we noticed rather strong lateral variation between arrivals recorded along the profile, which clearly illustrates the complexity of the structure.

3.2. Full Waveform Tomography Data Preprocessing

[43] Data preprocessing is a fundamental step for FWT. The two main objectives of data preprocessing are to improve the signal-to-noise ratio and to transform the data such that processed data reflect the approximations made in the wave propagation and inversion algorithms.

[44] The preprocessing sequence is composed of the following steps: (1) 3-D to 2-D correction of the observed data set (the amplitudes were scaled by $\sqrt{t}$, where t is time); (2) minimum-phase whitening (i.e., frequency domain deconvolution [*Yilmaz*, 2001, pp. 253–255]) (the amplitude spectrum of the deconvolution operator was normalized to preserve the original amplitude of data); (3) Butterworth band-pass filtering to improve the signal-to-noise ratio (the amplitude spectrum of the data before and after whitening plus Butterworth filtering is shown in Figure 5); (4) quality control and trace editing to remove noisy traces; (5) application of a reduced timescale to facilitate subsequent application of coherency filtering; (6) spectral matrix filtering to improve the signal to noise ratio and to strengthen the lateral coherency of traces; and (7) time windowing to mute water layer multiples. We did not make any attempt to process multiples from the free surface although the FD modeling code can account for these arrivals. In the case of diffraction tomography, free-surface multiples can be viewed as multiscattered signals. A least squares full waveform inverse problem accounts efficiently for these signals if a full Newton algorithm can be implemented (i.e., if the full Hessian can be inverted) [*Pratt et al.*, 1998]. Since we use a simple gradient algorithm, multiples may be misinterpreted as single-scattered arrivals leading to noisy tomographic images. Moreover, multiples carry no specific information on the medium and can be dominant in the cost function, hence excessively influencing the convergence of the inverse problem. Since multiples were muted, an absorbing upper boundary was used in the waveform modeling code.

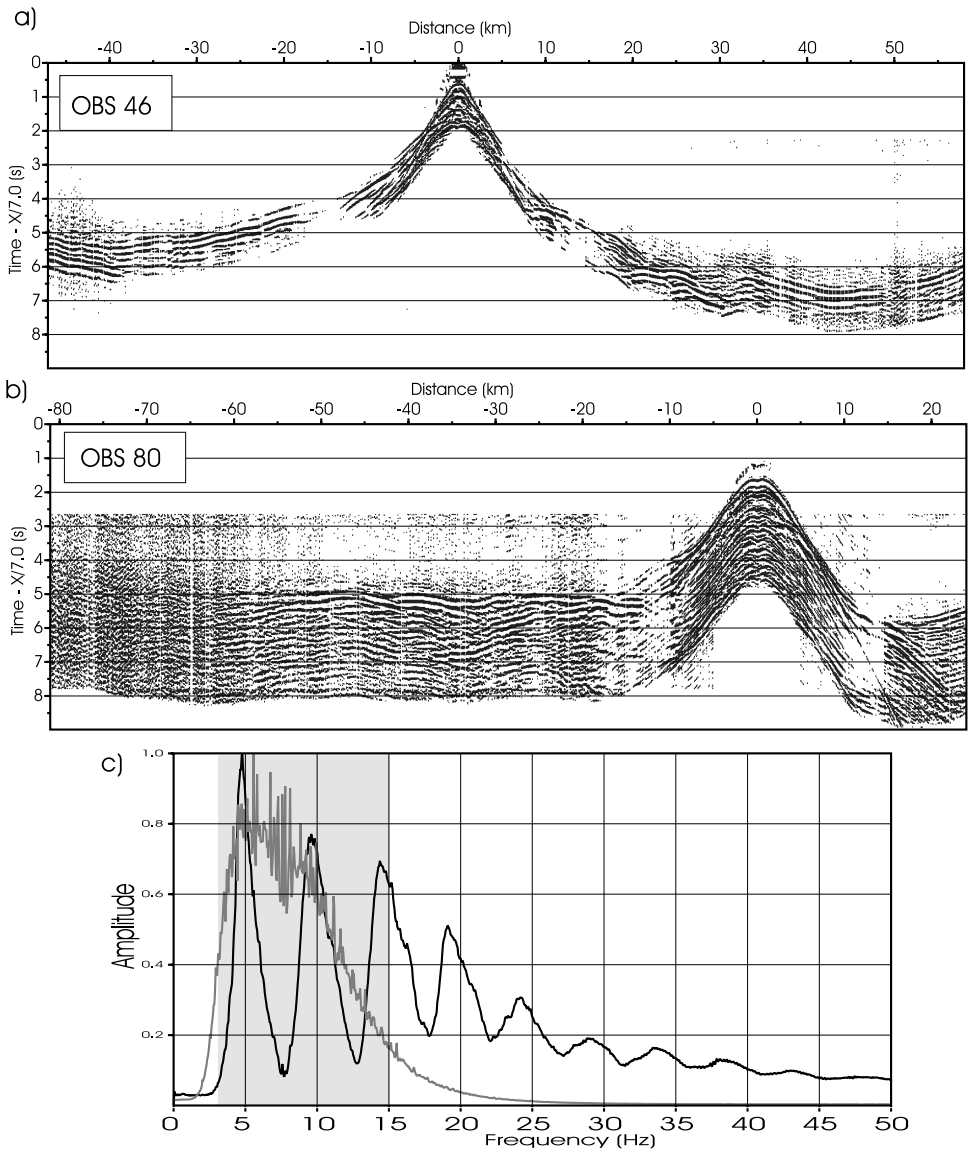

Figure 5. Two examples of OBS gather, (a) OBS 46 and (b) 80, after FWT preprocessing. The water depth is 700 and 3700 m on each gather. The width of the time window depends on the water depth, and its upper limit is just above the free surface multiple. (c) Spectral amplitude of the raw data (black curve) and the preprocessed data after whitening and Butterworth filtering (grey curve). The gray area delineates the range of frequencies involved in FWT.

[45] The spectral amplitude of the raw data exhibits several notches suggesting that frequencies such as 7, 8, 12, and 13 Hz are affected by a poorer signal-to-noise ratio (Figure 5c). These frequencies were raised by the spectral deconvolution leading to an overall degradation of the signal-to-noise ratio. This degradation was mitigated by subsequent Butterworth filtering. The good quality of the data after whitening and Butterworth filtering (Figure 4) suggests that the benefit of the deconvolution in terms of signal compression exceeds the inherent degradation of the signal-to-noise ratio it brings. As an illustrative example, the spectral deconvolution allows us to identify subtle phases such as T, Rbs, PB and IR which can hardly be seen prior to it (Figure 4a).

[46] Two examples of preprocessed OBS gathers are shown in Figures 5a and 5b. For deeply immersed OBSs, the time muting window can be made sufficiently wide to incorporate all the useful arrivals. In the case of shallow water, the time window is much more narrow and only wide-aperture components are preserved in the data. This must degrade the resolution achievable with FWT in the corresponding landward part of our model. A second problem raised by time windowing the data is that such processing cannot be applied easily to the single-frequency synthetic data computed in the FWT algorithm. Time windowing is a multiplication in the time domain, and hence a convolution in the spectral domain which would necessitate to model data for every frequency; this is precisely what we seek to avoid by working in the frequency

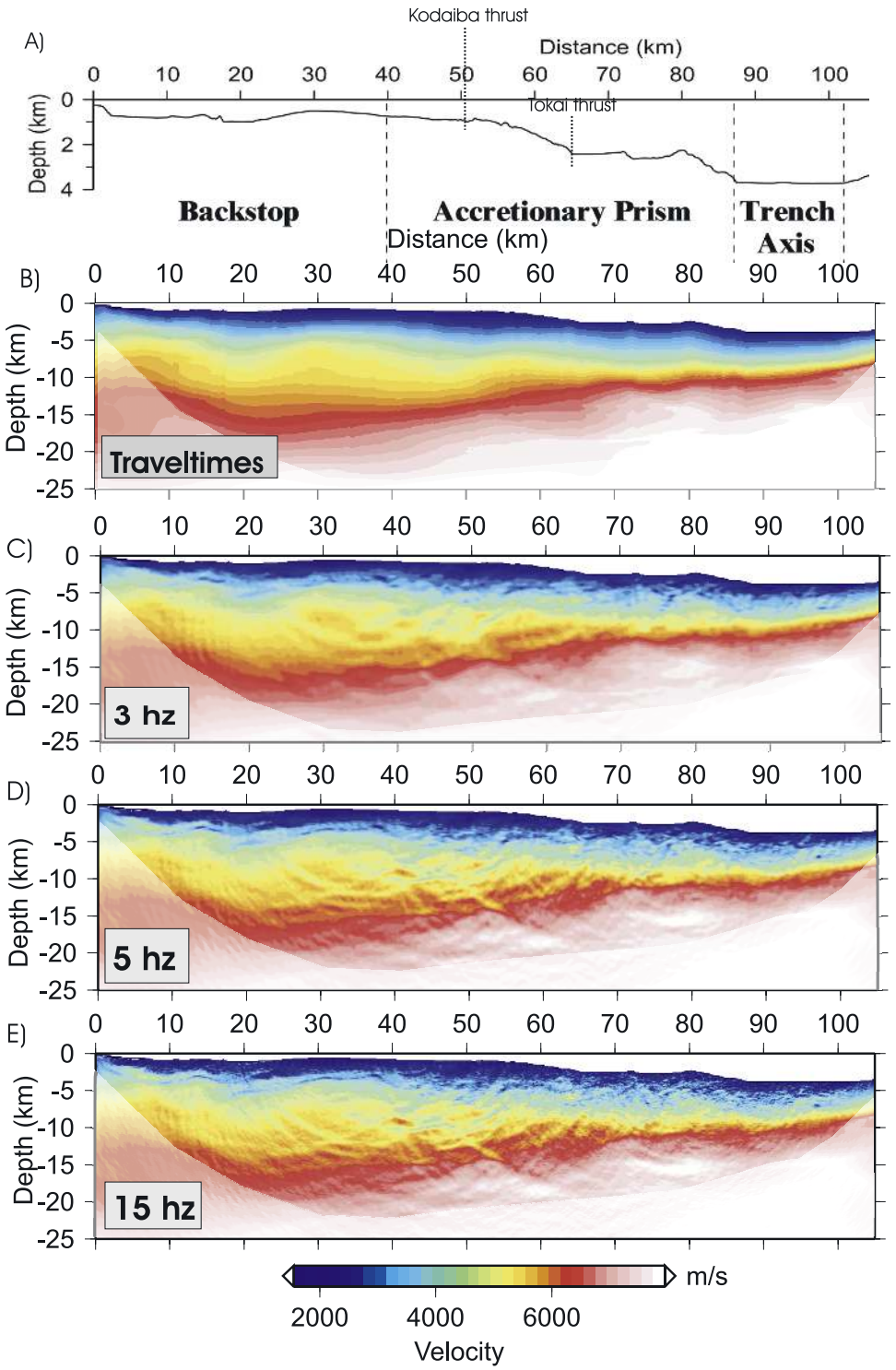

Figure 6. (a) Main domains of the subduction system. (b) FATT model used as initial model for FWT. FWT P wave velocity model after inversion at (c) 3 Hz, (d) 5 Hz, and (e) 15 Hz.

domain. Using properly tuned complex frequencies in the modeling to damp the signal in time [*Sirgue and Pratt*, 2004] is a possible alternative that we did not investigate here. In summary, we do not apply the same time windowing to the synthetic data computed throughout the inversion which is not a problem when the window is wide but which is more of an issue in the opposite case, as some information is incorporated in the synthetics whose equivalent in the observed data was removed and can therefore not be fitted.

3.3. Input Parameters and Computational Times of FWT

[47] The starting model for FWT was developed by FATT [*Dessa et al.*, 2004a] (Figure 6b). We sequentially inverted

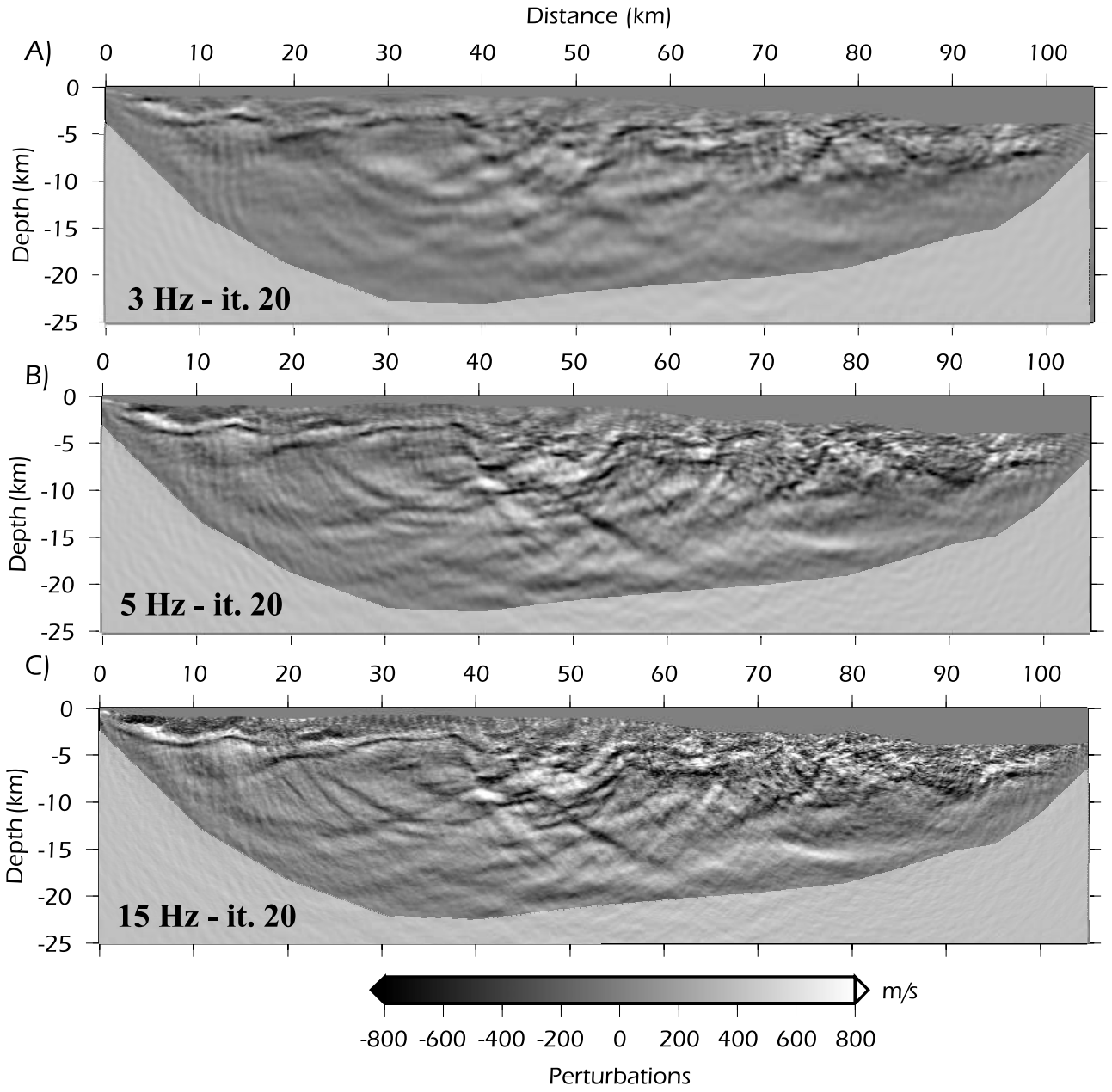

Figure 7. Perturbation models at (a) 3 Hz, (b) 5 Hz, and (c) 15 Hz.

13 frequencies uniformally sampled between 3 and 15 Hz with a 1-Hz interval. Although the components 7, 8, 12 and 13 Hz have a lower signal-to-noise ratio, we inverted them to maintain a sufficiently fine frequency interval in the data and thus an accordingly fine sampling in the wave number coverage. This 1-Hz interval is smaller than that predicted by a theoretical resolution analysis [*Sirgue and Pratt*, 2004] because it is difficult to predict the actual range of apertures that contribute to image a reflector in a real case. We defined the lowest inverted frequency (3 Hz) by trial-and-error. This frequency, albeit having a comparatively small spectral amplitude (Figure 5c), reveals meaningful features in the velocity models (Figures 6c, 7a, 8a, and 8b).

[48] We essentially tested 3 tuning parameters of FWT: the gain with offset g (8), the number of iterations per frequency and the correlation lengths of the smoothing operator. We tested $g = 1$ and $g = 0.5$ and qualitatively estimated that the P wave velocity perturbations obtained with $g = 1$ were those which were optimally scaled with depth. We performed two runs of FWT using 10 and 20 times per frequency, respectively. When increasing the iteration number, the velocity perturbations are sharper in most parts of the model but the signal-to-noise ratio may be degraded in other parts where the inversion failed to properly image the structures. In the following, we only show the results obtained after 20 iterations per frequency. The correlation lengths of the smoothing operator were heuristically chosen to obtain the best trade off between signal-to-noise ratio and resolution of the tomographic images. We also forced velocities to remain bounded between 1500 and 8300 m s^{-1}.

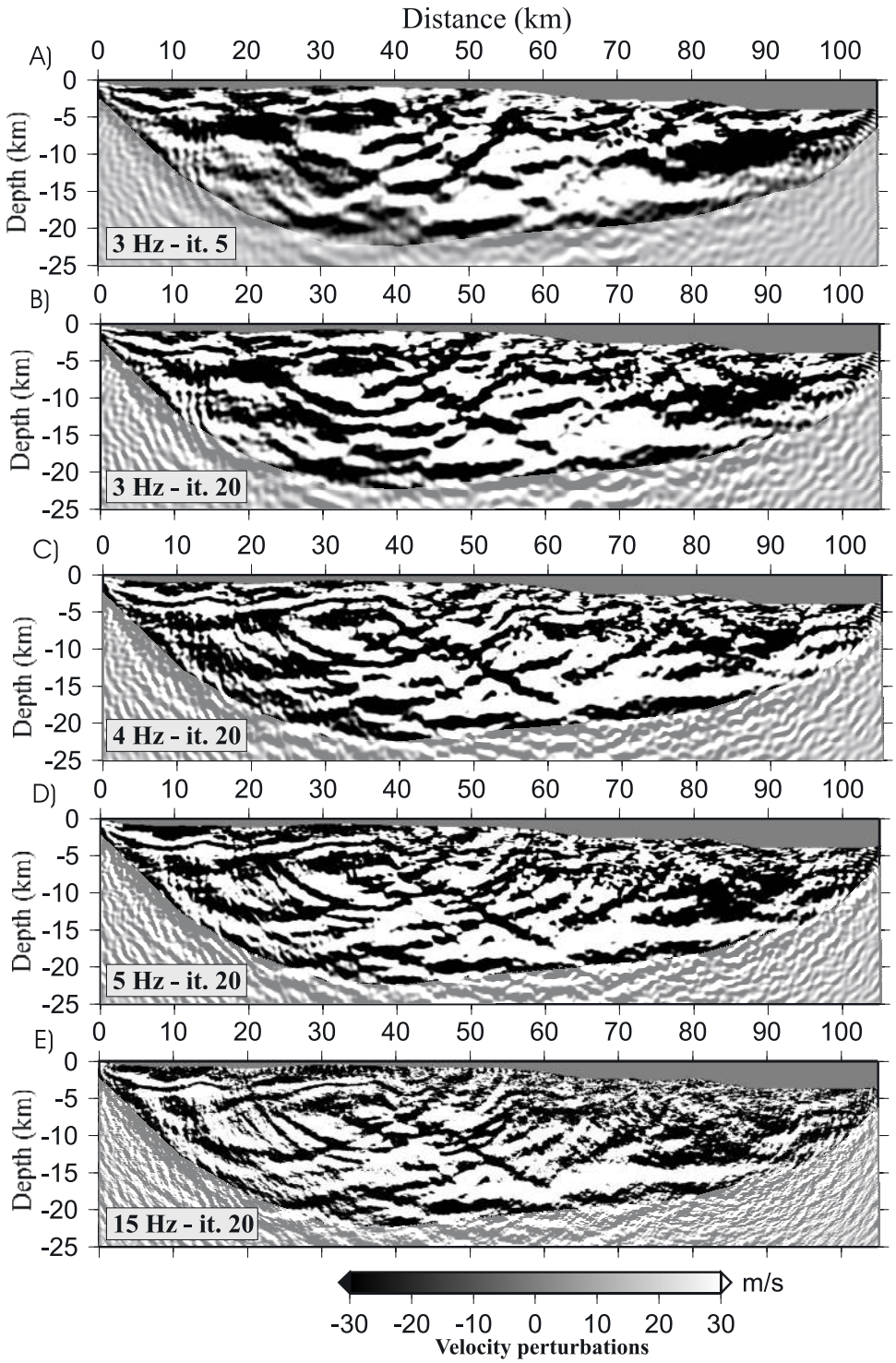

Figure 8. Perturbation models shown with a narrow gray scale spanning between −30 and +30 m s^{-1}. (a) Model at 3 Hz, iteration 5. (b) Model at 3 Hz, iteration 20. (c) Model at 4 Hz, iteration 20. (d) Model at 5 Hz, iteration 20. (e) Model at 15 Hz, iteration 20.

[49] We ran the FWT program on a Linux PC cluster. Six biprocessor nodes (twelve processors) with 4 Gb of RAM each were required to run the program. Eleven Gb of RAM were necessary to factorize the impedance matrix on the 6 nodes with the MUMPS solver [*Amestoy et al.*, 2000, 2001]. The total CPU time for completing 20 iterations for the 13 frequencies was more than 20 days. The model size is 105 km × 25 km to 4201 × 1001 FD grid with a 25-m grid step. This mesh spacing leads to a discretization of at least 4 nodes per wavelength, considering the range of velocities and frequencies explored here. Such sampling warrants accurate behavior of the FD wave propagation

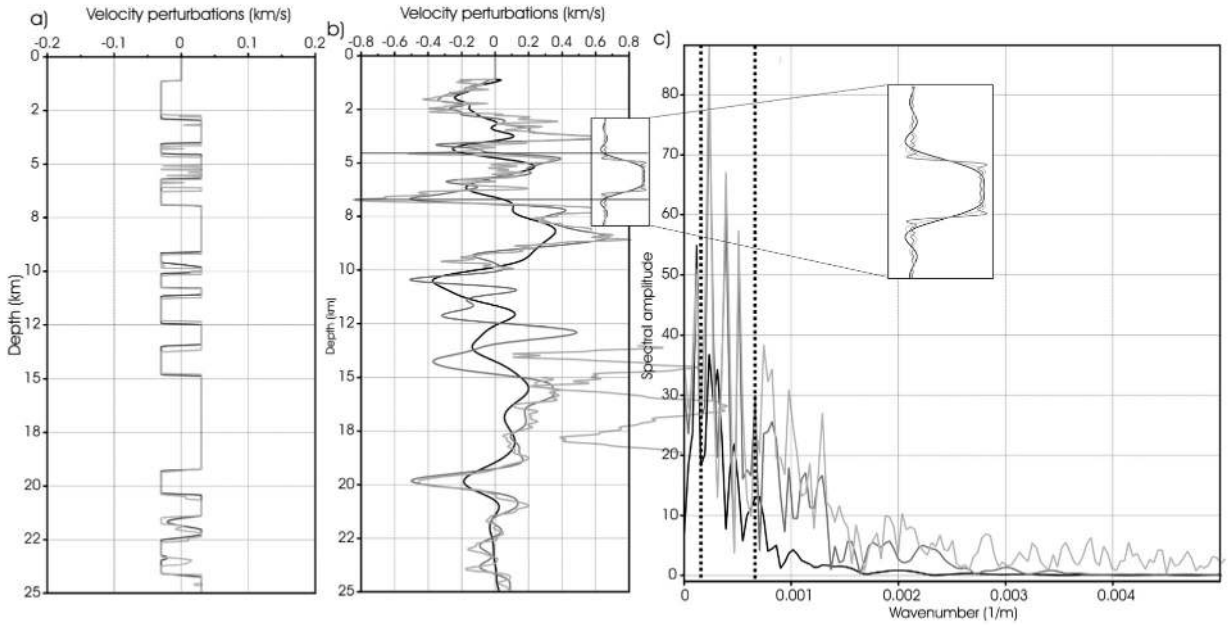

Figure 9. (a) Velocity perturbations along a log at 50 km after inversion at 5 Hz (black) and 15 Hz (gray) Hz. Perturbations are clipped within the same range as in Figure 8 (-30 m s^{-1}; $+30$ m s^{-1}). (b) Same as in Figure 8a with no clip. The inset shows a synthetic 2.7-km-thick layer, representative of the characteristic scale of the layering observed in the FWT profiles. A low-pass filter is applied to the synthetic profile with three cutoff wave numbers, defined to be representative of the theoretical resolution at 3 Hz (black), 5 Hz (dark gray), and 15 Hz (light gray). Note that for this layer thickness, the difference between the 5 and 15 Hz synthetic profiles is rather limited. Qualitative comparison between the synthetic and FWT profiles suggest that the three frequencies yield similar information. (c) Spectral amplitude of graphs shown in Figure 9b. The contribution of the 5-Hz component with respect to the 3-Hz one and of the 15-Hz component with respect to the 5 Hz are estimated to be wavelengths smaller than 4 and 1.4 km, respectively. These two limits are indicated by the thick dotted lines.

modeling [*Jo et al.*, 1996; *Hustedt et al.*, 2004]. We inverted 93 OBS gathers: each OBS gather contains 1050 traces before preprocessing. The gradient of the cost function and the resulting perturbation model were computed on a 1001 $\times$ 1001 grid with horizontal and vertical grid steps of 100 m and 25 m, respectively. The diagonal terms of the approximate Hessian in (7) were computed by keeping one trace out of four.

3.4. Full Waveform Tomography Results

3.4.1. Strategy for Interpretation and Appraisal of the FWT Results

[50] The velocity models obtained by FWT after inverting at 3, 5 and 15 Hz are shown in Figures 6c–6e. Since the crustal velocity models span a broad range of velocities (1.5–8.2 km s^{-1}), the interpretation of the structural discontinuities is difficult in an absolute velocity display. The specific contribution of FWT is better assessed from the difference between the output models and the initial one, obtained by FATT (Figures 7 and 8). These differential models are hereafter referred to as perturbation models.

[51] The perturbation models are shown in Figure 7 with a gray scale spanning velocity perturbations between -800 and 800 m s^{-1}. Narrowing the display range between -30 and 30 m s^{-1} favors the dominant wavelengths of the perturbation models at the partial expense of the spatial resolution and of the true amplitude of the velocity perturbations. The dominant scales of the geological layering typically ranges between 1 and 5 km (Figure 8). We superimposed one vertical profile extracted from the 5- and 15-Hz perturbation models at a horizontal distance of 50 km in Figures 9a and 9b with the two aforementioned display ranges (800 and 30 m s^{-1}). The comparison of the two sets of profiles illustrates the different nature of the information shown in Figures 7 and 8. The perturbation model at 3 Hz is shown after 5 (Figure 8a) and 20 (Figure 8b) iterations in Figure 8 to illustrate how the complexity and the signal-to-noise ratio of images evolve as iterations proceed for a single frequency.

[52] The main interpreted structural discontinuities are superimposed on the 4- and 15-Hz perturbation models and on the 15-Hz velocity model in Figure 10. They delineate large domains that are the subducting oceanic crust and the rigid backstop overlaid by the forearc basin deposits. The structural discontinuities were drawn from the combined analysis of perturbation models with different resolution levels (Figure 8) and the vertical profiles extracted from the FWT (absolute) velocity models (Figure 11). Perturbation models provide a suitable display to delineate tectonic discontinuities, just as depth-migrated sections. The additional analysis of absolute P wave velocity estimates allows us to propose hypotheses regarding geological units, their lithologies and the physical properties of discontinuities separating them. The interpretation of absolute values of

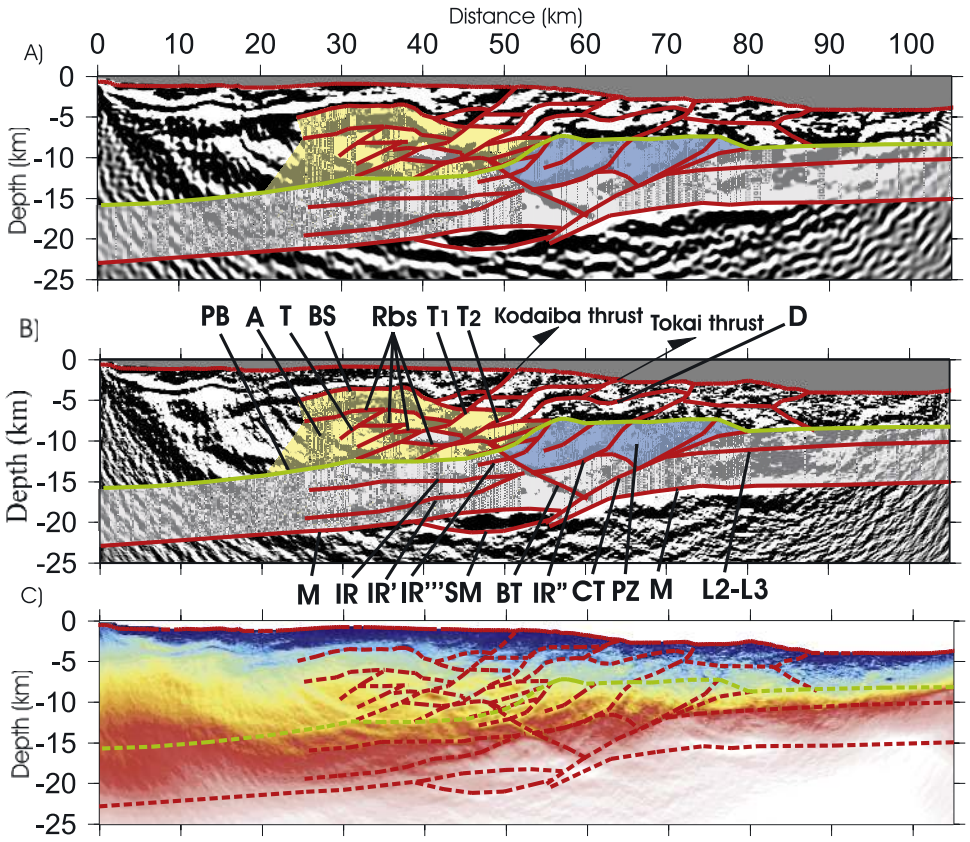

Figure 10. (a) The 3 Hz and (b) 15 Hz perturbation models. (c) Final FWT model. The structural interpretation is superimposed. The gray shaded area delineates the subducting oceanic crust. The blue shaded area delineates the Paleo-Zenisu body on top of the subducting oceanic crust. The yellow shaded area is the backstop. Nomenclatures are M, Moho; BS, top of backstop; Rbs, major reflector in the backstop; T, T1, T2, thrusts affecting the backstop; PZ, Paleo-Zenisu ridge; L2-L3, oceanic layers 2 and 3 of the subducting oceanic crust; D, décollement; Tokai, Tokai thrust; Kodaiba, Kodaiba thrust; CT, thrust affecting the subducting oceanic crust; BT, back thrust; PB, plate boundary (green line) (the plate boundary is assumed to lie on top of the Paleo-Zenisu body); IR,IR′,IR″,IR‴, intraoceanic crustal reflectors; SM, zone of possibly partially serpentinized mantle; A, artifact; HV, off-scraped high-velocity body.

the velocity must be done cautiously, as these values are possibly affected by errors caused by the use of the acoustic approximation as well as by intrinsic limitations in resolution.

[53] Classically, we draw the discontinuities by closely following the boundaries in the perturbation models. In some ambiguous cases, we also used the geological likelihood of the different possibilities. Such ambiguities may for instance be due to small velocity contrasts across interpreted boundaries or to possible low-velocity zones whose complex seismic signature renders the interpretation questionable. An illustrative example is the seismogenic portion of the plate boundary (PB), landward of the Paleo-Zenisu ridge, where the subducting oceanic crust is in contact with the backstop presumably composed of old indurated accretionary wedge (Figures 10 and 11b–11g). This portion of the reflector (PB) was inferred from our a priori knowledge of the thickness of standard oceanic crust and assuming a roughly constant crustal thickness prior to deformation. Other sources of ambiguities are noise and artifacts. For example, we did not interpret some bright features dipping oceanward that can be seen on the landward part of the perturbation models (labeled A in Figure 10) which may result from the inaccuracy in the corresponding part of the starting model, due to insufficient ray coverage during FATT (see the shaded areas in Figure 8). These inaccuracies may have been spread into the velocity model during FWT because of the spatial extent of the FWT sensitivity kernel.

[54] To appraise the relevance of the velocity models, we designed a practical approach based on forward modeling of traveltimes and waveforms. Once structural discontinuities were delineated, ray tracing of first arrivals and reflections was performed in the final FWT model with a FD eikonal solver [*Podvin and Lecomte*, 1991] (Figures 12–15). First-arrival ray paths are instructive because they tend to be channelled along the laterally coherent small-scale high-velocity features of the model and thus to behave like head waves along interfaces. This agreement between the trajectory of head wave rays and the digitized interfaces validates the structural interpretation. Moreover, we verified the fit between the first-arrival traveltimes computed in the FWT models and the observed ones, which provides a strong

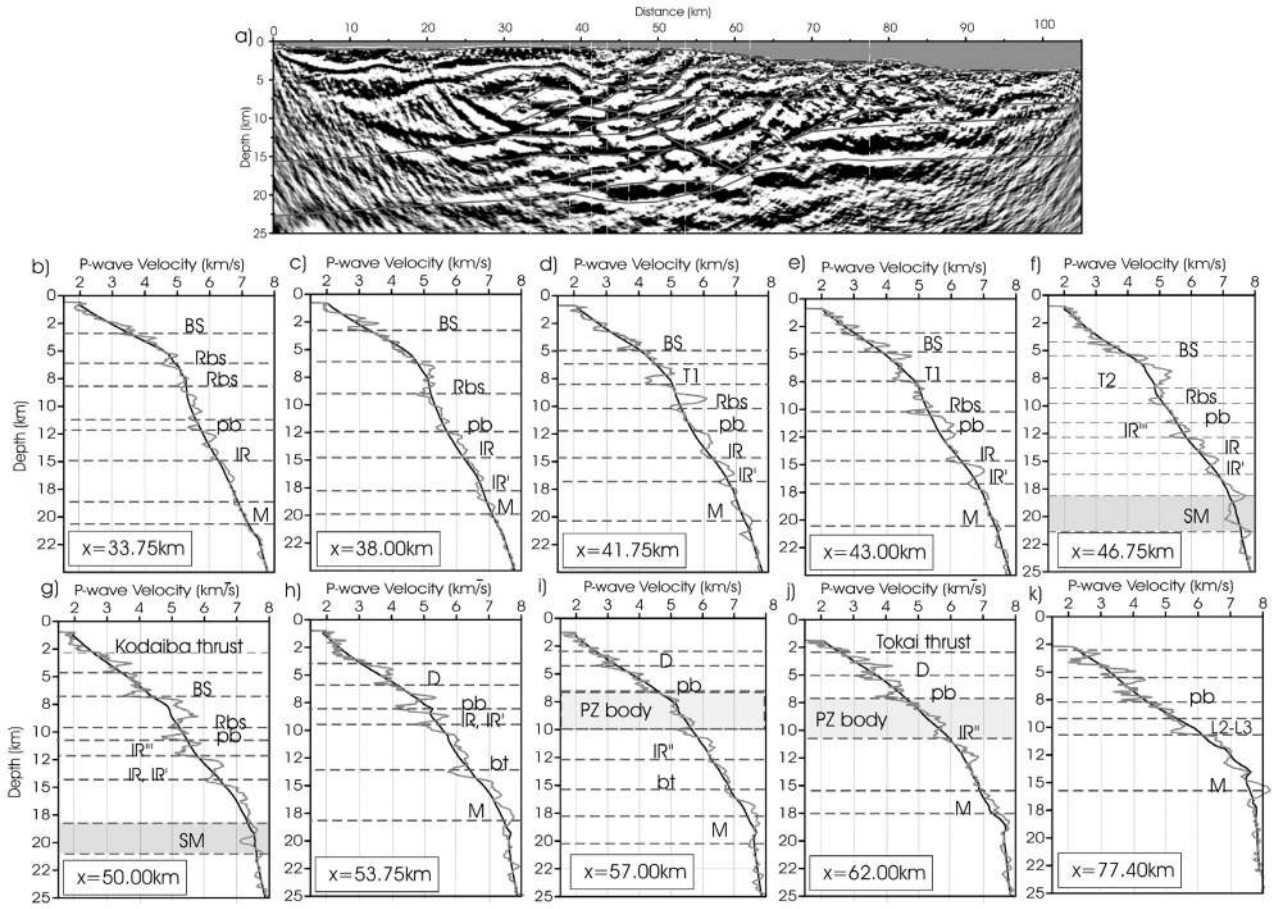

Figure 11. (a) The 15 Hz perturbation model with superimposed structural interpretation. We slightly high-pass filtered the perturbation model to facilitate delineation of reflectors such as the plate boundary and intracrustal reflectors IR and IR′ between 30 and 45 km (compare Figures 11a and 10b). Delineation of the top of the oceanic crust and the layer 2/layer 3 interface is also easier in Figure 11a compared to Figure 10b. The vertical dashed lines give horizontal positions of the vertical profiles shown in Figures 11b. (b) Series of P wave velocity logs extracted from the FATT (black line) and the final 15 Hz FWT (gray line) models (Figure 6e). The horizontal lines mark the depth of the interfaces superimposed to the perturbation model in Figure 11a. Nomenclature is the same as that of used in Figure 10.

argument to state that the FWT did not converge toward unrealistic local minima and was not significantly affected by cycle skipping artifacts (Figure 16). The ray tracing of reflections was computed for a selection of digitized interfaces (Figures 12–15) and the resulting traveltimes were superimposed on the OBS gathers to test whether they fit some observed reflections (Figure 16).

[55] We assessed the efficiency of the waveform fitting procedure and the amplitude calibration by comparing the observed and computed single-frequency data for some representative OBS gathers (Figure 17). Real part of observed and computed data are superimposed at iterations 1 and 20 to assess the sensitivity of the seismic data to the perturbations incorporated during the inversion of one frequency. For example, the difference between the 4 and 5 Hz perturbation models (Figures 8c and 8d) led to the fit improvement at 5 Hz shown in Figure 17. Data are plotted in Figure 17 after applying the operator $\mathbf{W}_d$ to assess the relative weight of each class of offsets in the inversion.

[56] Time domain FD synthetic seismograms allow a more familiar interpretation of individual phases but the comparison between observed and computed seismograms remains qualitative in the absence of a reliable estimate of the source wavelet in the time domain (Figure 18). We computed the seismograms in the FATT and FWT models to provide a second illustration of the sensitivity of the data to the velocity perturbations reconstructed by FWT. We used a smoothed temporal delta function as the source term, which should be a good approximation for deconvolved data. The delta function was band-pass filtered just like the real data (Butterworth filtering).

3.4.2. Geological Description of the FWT Velocity Models

3.4.2.1. Subducting Oceanic Crust

[57] The subducting oceanic crust is delineated by the gray shaded area in Figure 10. The blue area on top of the oceanic crust marks the so-called Paleo-Zenisu (PZ) body. The western flank and top of the ridge are clearly imaged on the different perturbation models (Figure 8). The eastern

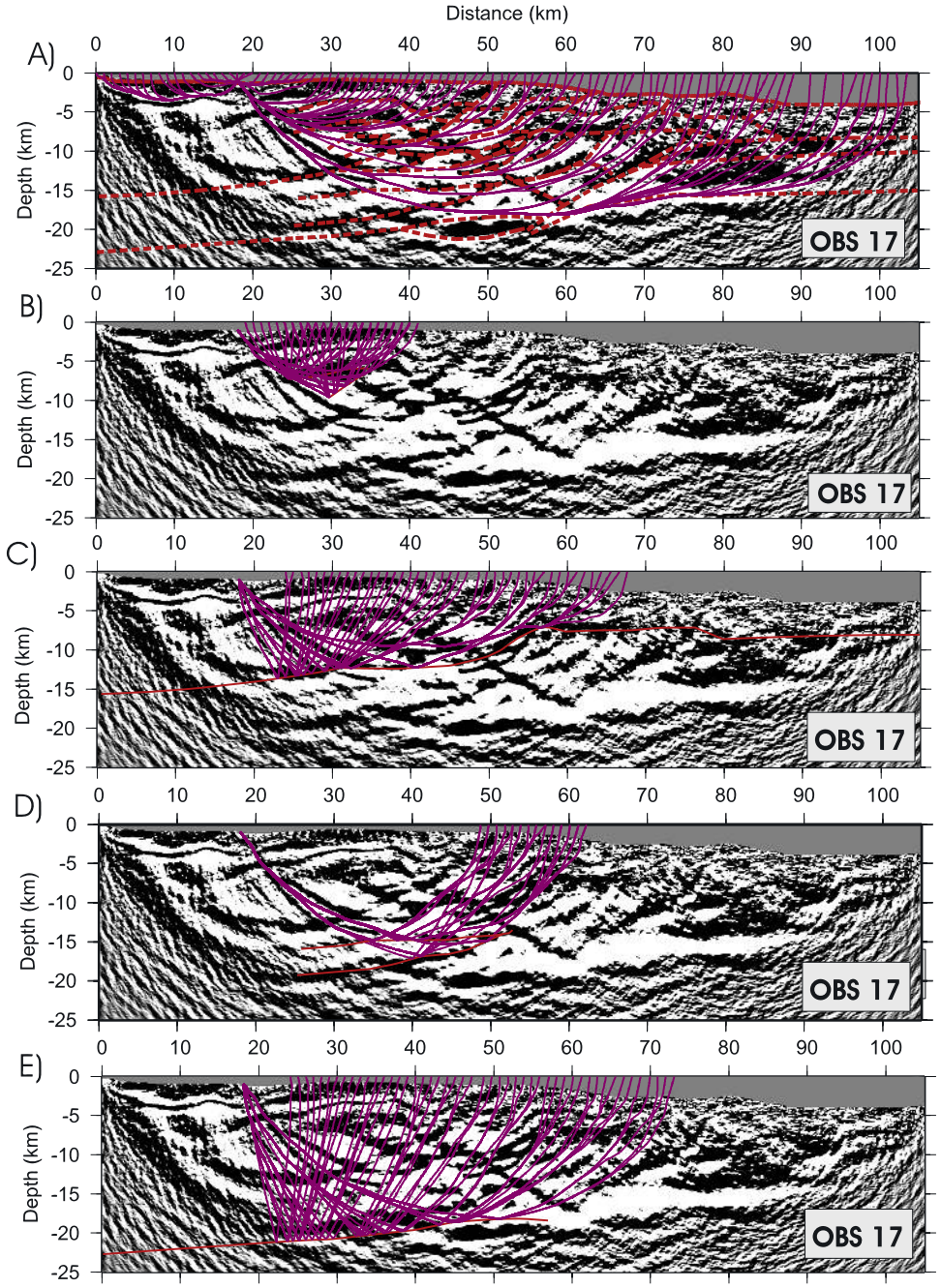

Figure 12. (a) First-arrival and (b–e) reflection ray tracing for OBS 17. Reflection ray paths were computed for those reflectors whose seismic response was identified in the observed data (Figure 21). These reflectors are Rbs (Figure 12b) and T. The plate boundary (PB) (Figure 12c), the intracrustal reflectors IR and IR′ (Figure 12d), the Moho (M) (Figure 12e). The refraction and reflection ray paths are superimposed on the perturbation models rather than on the absolute velocity models from which they are computed to highlight the relationship between ray trajectories and structural discontinuities.

flank of the Paleo-Zenisu ridge is more affected by noise. To our knowledge, the perturbation models of Figure 8 have provided the clearest picture of this ridge since its existence was first proposed by *Lallemand et al.* [1992]. The top of Paleo-Zenisu ridge was interpreted as a décollement level by *Le Pichon et al.* [1996], which is supported by the low-velocity anomaly imaged on top of the ridge (Figures 11h–11j). In agreement with *Le Pichon et al.* [1996], our results clearly support that the top of the Paleo-Zenisu ridge delineates the plate boundary (PB) between horizontal distances 55 and 75 km in Figure 10. The position of the ridge is also consistent with that proposed by *Le Pichon et al.* [1996]. The hypothesis that the ridge would have been off-scraped and that its bottom would now mark the boundary is definitely ruled out. A second reflector, referred to as D in Figure 13, can be proposed as a second décolle-

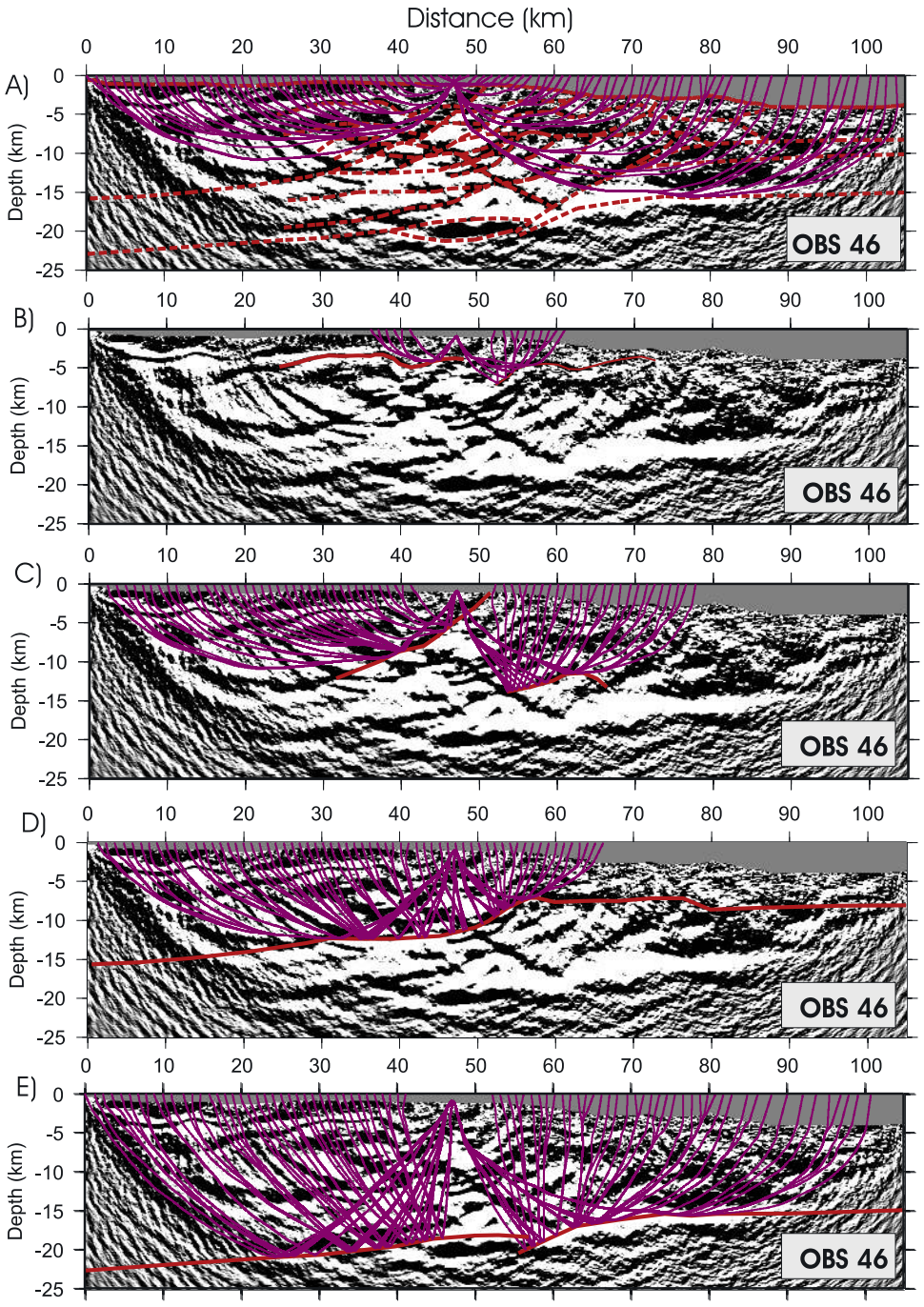

Figure 13. (a) Same as Figure 12 but for OBS 46. The modeled reflectors are (b) the top of backstop BS and décollement D; (c) the thrust T1 and the base of the Paleo-Zenisu body IR″; (d) the plate boundary segment corresponding to the landward flank of the Paleo-Zenisu ridge and the upper part of the seismogenic zone; and (e) the Moho M.

ment above the Paleo-Zenisu ridge, but our results are not of sufficient resolution to assess the tectonics in the sedimentary wedge and to discuss that point; MCS images are necessary for this. Velocities in the upper crust range between around 4.5 and 5.7 km s^{-1} in Figure 11j, which is in agreement with those found by *Nakanishi et al.* [1998] (4.5–5.6 km s^{-1}) in the upper crustal layer of the analogous Zenisu ridge located just seaward of the trench (Figure 3).

[58] Several reflectors were imaged in the subducting oceanic crust (IR, IR′, IR″, IR‴,CT, BT, L2-L3 in Figures 10 and 11). The reflector L2-L3 is interpreted as the layer 2/layer 3 interface. This reflector corresponds to a velocity jump from 5–5.5 km s^{-1} at the base of the layer 2 to 6.5 km s^{-1} on top of layer 3 (Figure 11k). A reflection from the layer 2/layer 3 interface is clearly visible in the OBS gathers located near the seaward end of the profile (Figure 4d). Reflectors CT and BT are interpreted as

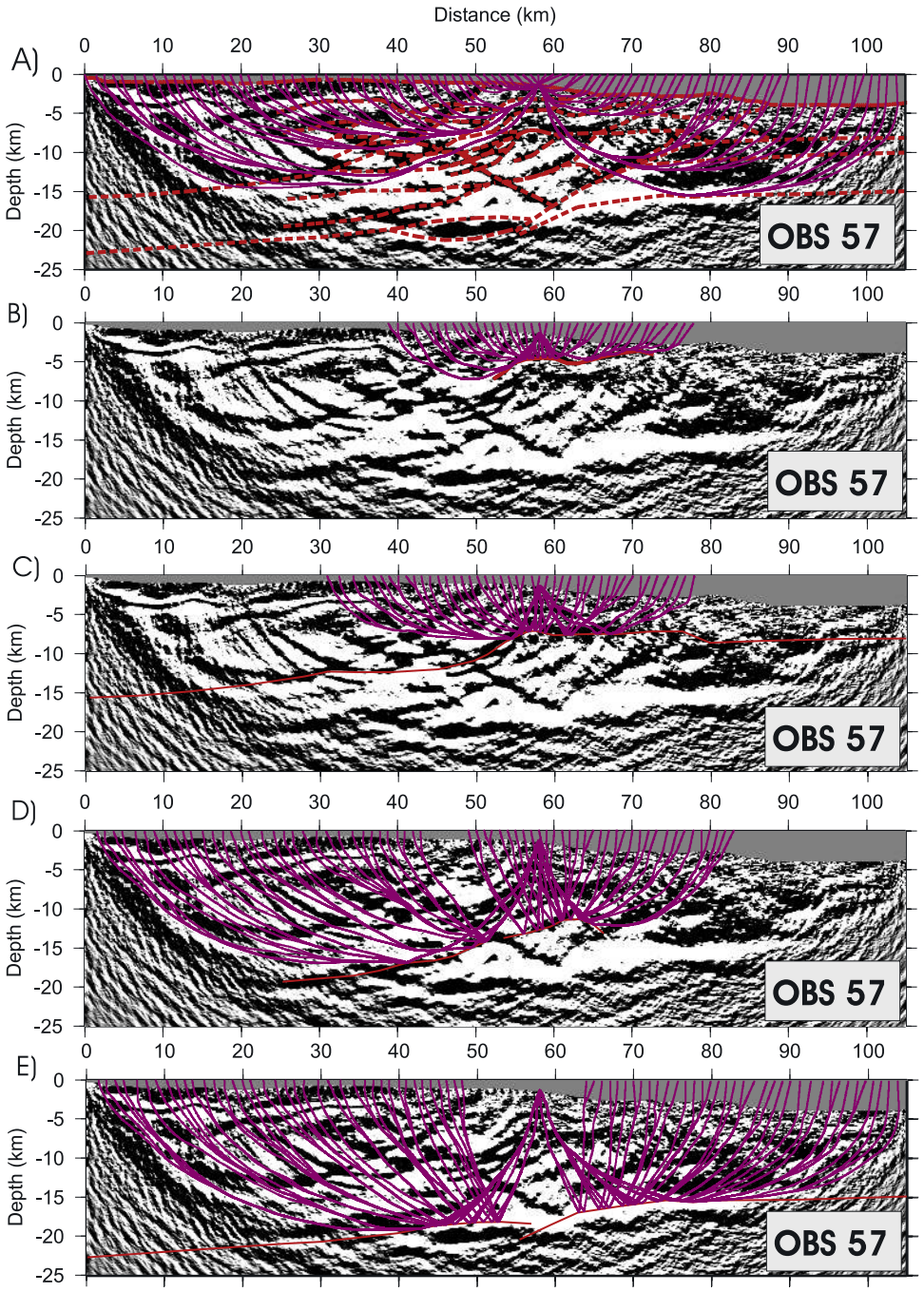

Figure 14. (a) Same as Figure 12 but for OBS 57. The modeled reflectors are (b) the décollement D, (c) the plate boundary segment corresponding to the top of Paleo-Zenisu ridge for this range of distances, (d) the intracrustal reflectors IR′ and IR″, and (e) the Moho.

major thrust and backthrust affecting the whole crust [*Dessa et al.*, 2004a]. The strong compression experienced by the oceanic crust when approaching the subduction [*Lallemant et al.*, 1989] is responsible for this large-scale thrusting that is possibly still active when entering the subduction. The crustal thrust CT is better imaged at 3 Hz in Figure 8a. Two intracrustal reflectors IR and IR′ are observed in the subducting oceanic crust landward of the Paleo-Zenisu ridge (Figure 10). These two reflectors seem to connect at 50 km of distance. The reflector IR can be interpreted as the layer 2/layer 3 interface and seems to prolongate in the Paleo-Zenisu ridge (see reflector labeled IR″ in Figure 10). The second landward dipping interface IR′ is somewhat more enigmatic. While the IR reflector marks a positive velocity jump between ~6 and 7 km s^{-1}, IR′ marks a low-velocity anomaly beneath IR (Figures 11d–11g). Furthermore, this reflector seems to flatten landward and to eventually root on the Moho at ~30 km of distance (Figures 10 and 11d–11g). This interpretation would imply a softening of the material and possibly

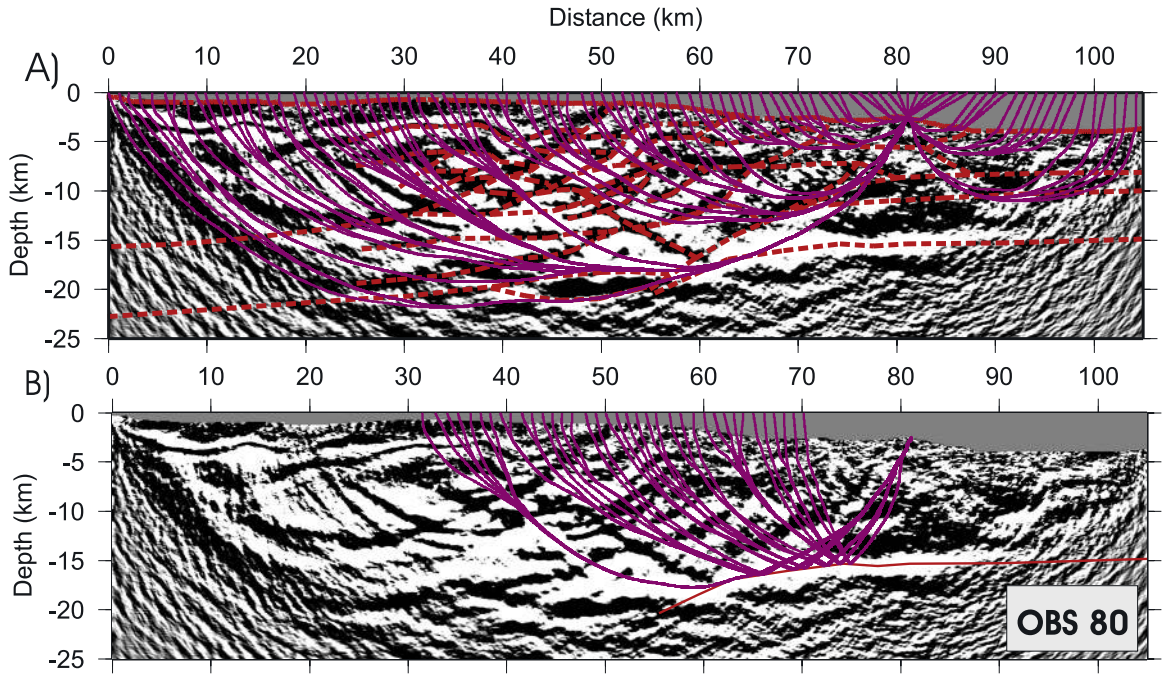

Figure 15. Same as Figure 12 but for OBS 80. The modeled reflector is the Moho (Figure 15b).

a transition to ductile rheologies whose most obvious origin in this context could be serpentinization resulting from hydrothermal alteration. This hypothesis would however imply that the oceanic crust itself embeds a significant part of ultramafic material, as proposed in slow to ultraslow oceanic accretion by *Cannat* [1996]. Such discussion is speculative and beyond our scope here. We just stress that the reconstruction of IR and IR′ is shown to correspond to energetic wide-angle reflections observed in Figures 16c and 18c.

[59] Our images suggest a direct contact of the Paleo-Zenisu ridge at its landward limit with the seaward limit of the backstop at ~50 km. At this location, the plate boundary shows a marked low-velocity anomaly from ~5.5 to ~4–4.7 km s^{-1} (Figures 11g and 11h). Prior to this study, low velocities (3–4 km s^{-1}) were reported at the top of the plate boundary beneath island arc crust [*Kodaira et al.*, 2002; *Mochizuki et al.*, 2005; *Kodaira et al.*, 2004] which were interpreted as the result of the presence of water [*Kodaira et al.*, 2002] or clay minerals and/or serpentinite-chlorite [*Mochizuki et al.*, 2005].

[60] On the basis of constraints from various active margins including other segments of the Nankai trough, it was proposed that the seaward limit of the backstop marks the upper limit of the seismogenic zone which would thus be located about 40 km landward of the subduction front [*Dessa et al.*, 2004a]. The structure of the subducting oceanic crust at this place appears to be more complex than the layered idealization that is usually retained. This likely is the footprint of the Paleo-Zenisu ridge that confers an anomalous character to the oceanic crust with in particular, a compressive tectonics that thickens it and arguably, some overprinted volcanism. Landward of the Paleo-Zenisu ridge, the plate boundary is more difficult to draw probably because of a small velocity contrast between the overlying plate and the subducting oceanic crust. Our interpretation of this interface yields velocities in the layers 2 (i.e., between reflectors PB and IR) and 3 (i.e., between reflectors IR and M) ranging between ~5.5 and ~6.2 km s^{-1} and between ~6.2 and ~7 km s^{-1}, respectively (Figures 11b–11f).

3.4.2.2. The Backstop

[61] The backstop is delineated by the yellow area overlaid by the forearc basin deposits (Figure 10). Its proposed upper limit correlates with that of the Shimanto wedge as defined by *Martin* [2003], based on coincident multichannel seismic reflection data. The top of the backstop corresponds to a velocity contrast between 3–3.5 km s^{-1} at the base of the forearc deposits and 4–4.5 km s^{-1} on top of the Shimanto wedge (Figures 11b–11e). The Shimanto belt is presumably composed of old accreted sediments resulting from the ancient subduction of the Pacific plate beneath the Japanese arc, before the opening of the Philippine sea plate. We have also included in the definition of the backstop the units located oceanward of the Kodaiba thrust that were interpreted as the Miocene wedge by *Martin* [2003].

[62] The backstop has experienced important compressive tectonics, illustrated by the thrusted structures that affect it [*Dessa et al.*, 2004a]. This intense compressive regime may result from cyclic ridge subduction [*Kodaira et al.*, 2003]. The thrusts affecting the backstop correlate with negative velocity anomalies, suggesting the presence of lower rigidity materials (Figure 11). The most likely hypothesis for that is the existence of fluid circulation along fault-induced paths and the presence of gouge and damaged fault zones at depth. A major reflector Rbs is imaged in the backstop and was already imaged by prestack depth migration [*Dessa et al.*, 2004a]. This reflector exhibits several offsets resulting from thrusting evidenced by the thrusts T and T1 in Figure 10 and corresponds to a zone of average velocity 5–5.5 km s^{-1}. It was proposed to be a diagenetic to low-grade metamorphic front in the Shimanto unit [*Dessa et al.*, 2004a].

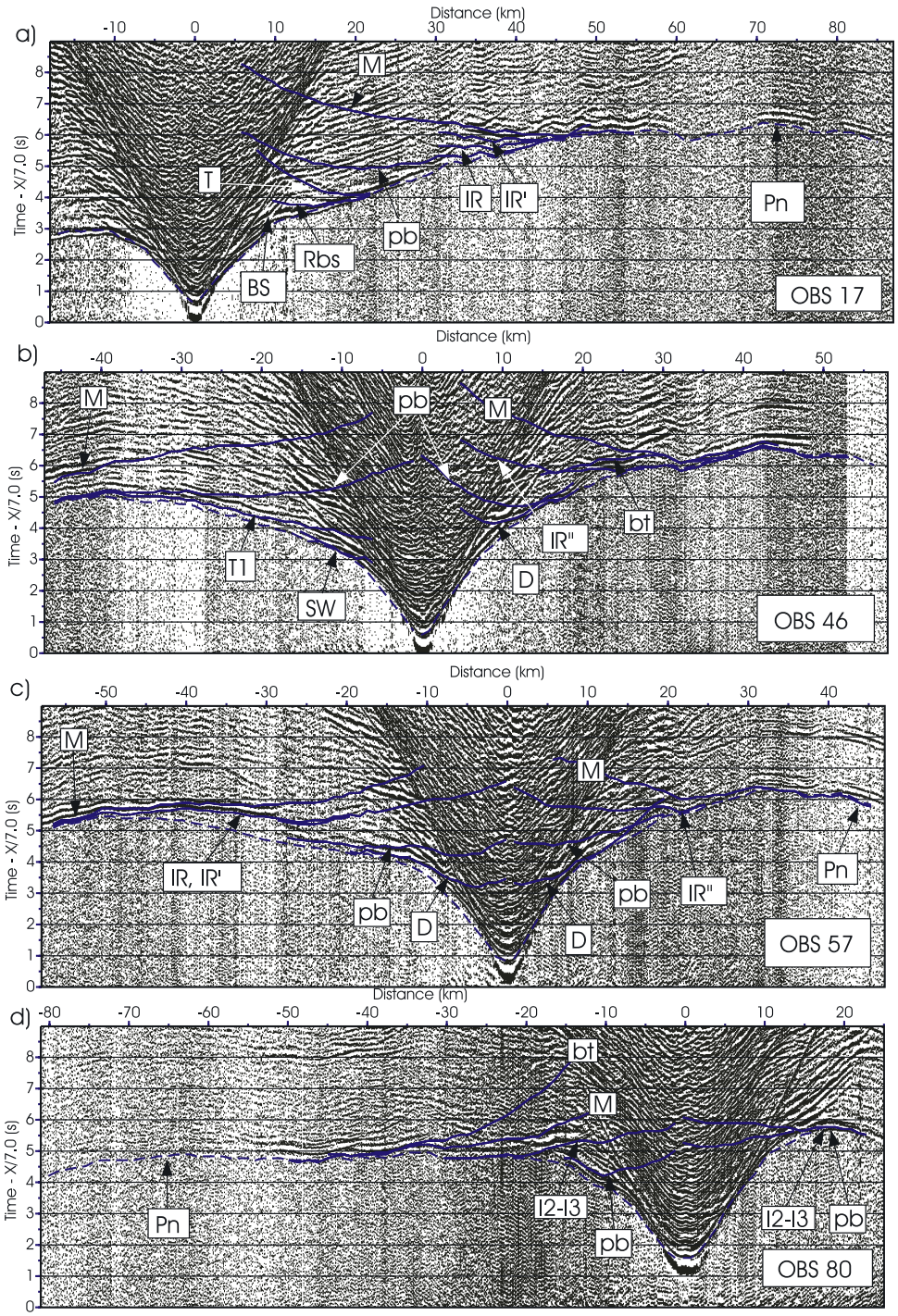

Figure 16. OBS gathers (a) 17, (b) 46, (c) 57, and (d) 80 with superimposed first-arrival refraction and reflection travel time curves. The refraction traveltime curves are dashed lines. The reflection traveltime curves are labeled by the associated reflector abbreviation (Figure 10).

[63] The major thrust T1 reaches the sea bottom at the position of the Kodaiba thrust. This thrust which is rooted on the seismogenic part of the plate boundary (PB) may act as a splay fault during great subduction earthquakes such as the anticipated Tokai earthquake. To our knowledge, our models have provided the first images of the prolongation in depth of the Kodaiba thrust down to the upper part of the seismogenic zone.

[64] A high-velocity body (HV) with a velocity of 6 km s^{-1} was imaged below the thrust T1 at a distance of 40 km (Figures 10 and 11d). The velocity of this body is significantly higher than the velocities in the adjacent units and is comparable to that observed on top of the subducting oceanic crust (compare profiles of Figures 11c–11e). Therefore this body may be proposed to consist in off-scraped oceanic crustal material accreted to the backstop.

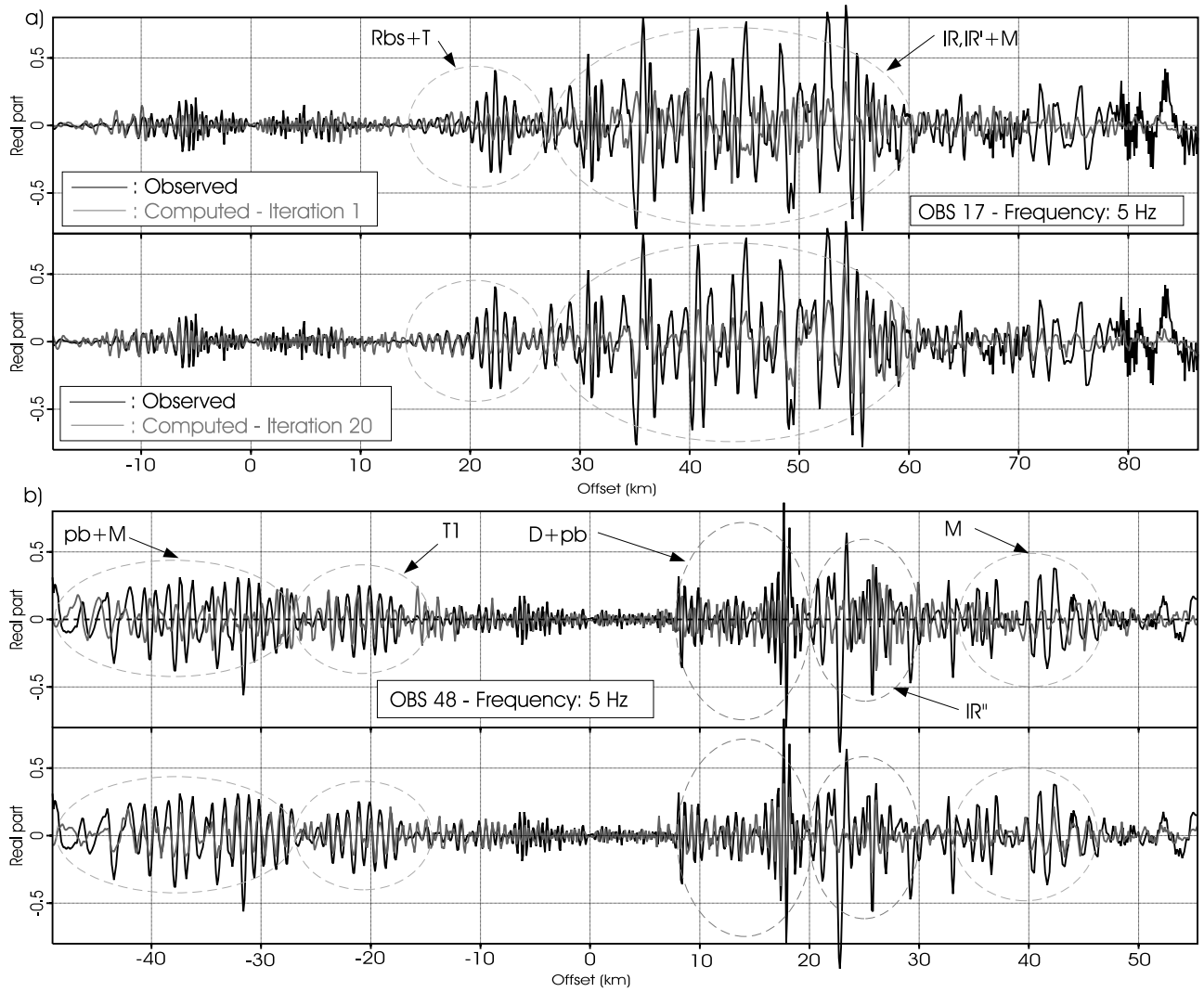

Figure 17. Comparison between the real part observed (black) and computed (gray) data at a given frequency as a function of offset for four OBS gathers (a) OBS 17, (b) OBS 48, (c) OBS 57, and (d) OBS 80. The frequency is 5 Hz. The top and bottom panels show the synthetic data at iterations 1 and 20, respectively. The dashed lines delineates signals corresponding to individual or group of dominant arrivals in the data.

[65] An analysis of velocities in the upper mantle from land to ocean suggests an overall increase from typically 7.5 to 8.2 km s^{-1} (Figures 11b–11k). This is consistent with a large-scale process of mantle serpentinization which would take place landward of the subduction front where the compressive regime created by the subduction of the Paleo-Zenisu ridge has created large-scale thrusts and therefore a path for bringing water down to the upper mantle.

3.4.3. Forward Modeling of OBS Gathers

[66] We now present several illustrations of the data fit for 4 representative OBSs along the profile (OBSs 17, 46, 57 and 80) which are located at 18, 47, 58, and 81 km of distance in order to assess the relevance of the structural features introduced above (Figure 10).

3.4.3.1. Modeling of OBS17

[67] The short-offset seismograms show three refracted arrivals between offsets ~2–5, 5–10, and 10–30 km, respectively (Figure 4a). Ray paths suggest that the two firsts were refracted in the deposits of the forearc basin and that the third was refracted in the upper part of the Shimanto wedge, down to the Rbs reflector (Figure 12a). A shadow zone is observed between offsets ~30 and 55 km suggesting a small velocity gradient from Rbs to the bottom of the subducting oceanic crust. This is confirmed by the vertical profiles of Figures 11b–11e which indicate a sharp decrease of the velocity gradient below ~5–7 km depth. The subhorizontal ray paths between distances of ~35 and 50 km closely follow the plate boundary landward from the Paleo-Zenisu ridge (Figure 12a). These rays reach the surface at distances between 62 and 68 km, which corresponds to offsets between 44 and 50 km in Figures 4a and 16a. At these offsets, a very weak first arrival is observed before a strong wide-angle reflection suggesting that it corresponds to the refraction from the top of the subducting oceanic crust. The reflected ray paths and traveltimes suggest that the strong wide-angle reflection is formed by the assem-

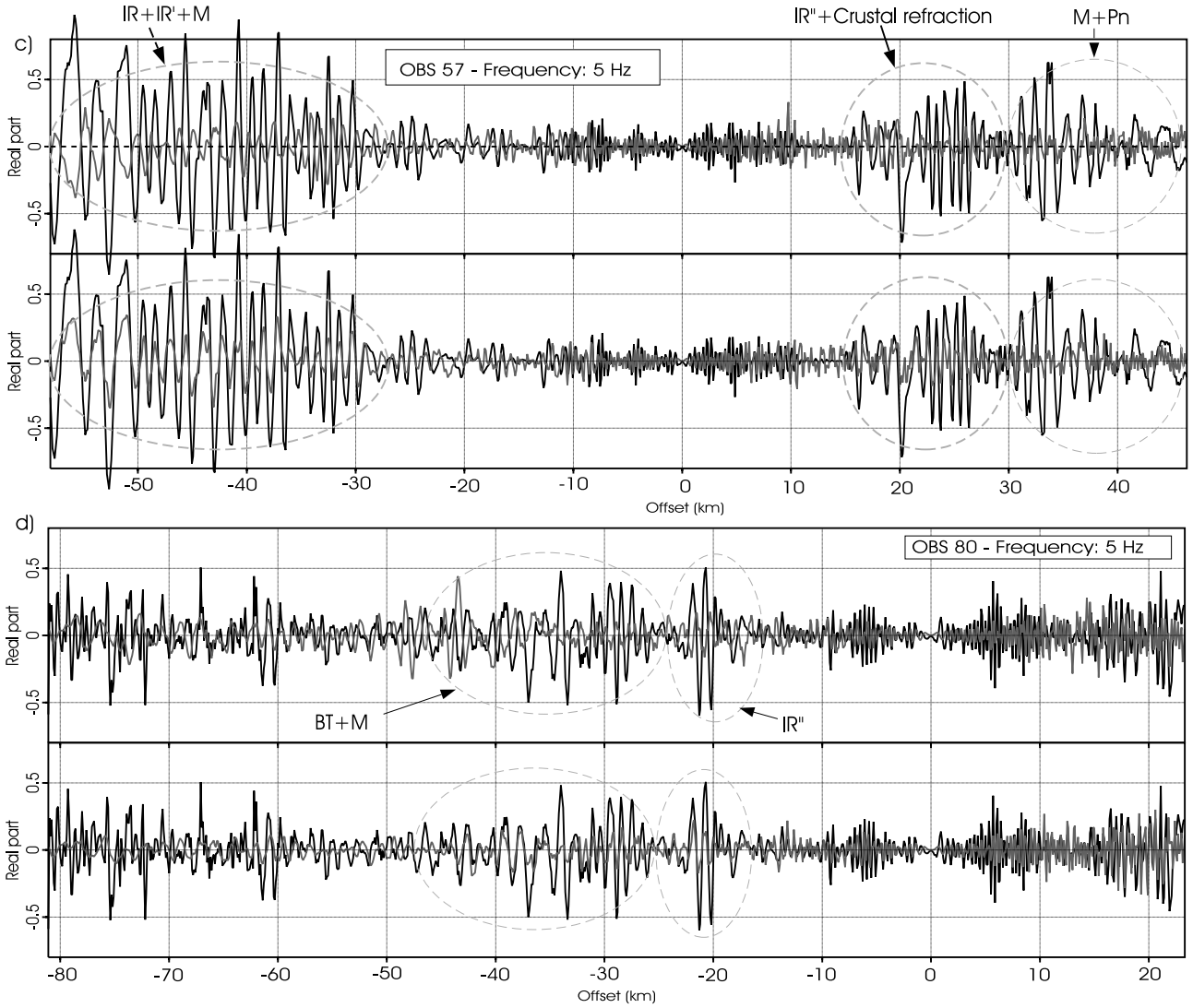

Figure 17. (continued)

blage of the reflection from the intracrustal reflector IR′ and from the Moho (Figures 12d, 12e, and 16a). The Pn wave (i.e., upper mantle refraction) is observed between offsets ~55 and 87 km. The 55-km offset is consistent with that corresponding to the shortest-offset ray refracted in the upper mantle in Figure 12a. Reflections from the plate boundary and from the intracrustal reflector IR are rather subtle in the data (Figure 4a) but the modeling of their travel times allowed us to interpret these events in the data (Figures 12c, 12d, and 16a). The refraction ray paths allow us to properly delineate the Moho between distances 40 and 90 km (Figure 12a). Two other subtle reflected and/or diffracted arrivals labeled Rbs and T are observed in Figure 4a which may correspond to the seismic response of the Rbs reflector and the thrust T (Figures 12b and 16a).

[68] A cost function reduction of 50% was reached for OBS 17 and frequency 5 Hz (Figure 19b). The 5-Hz data fit is shown in Figure 17a. We indicated in Figure 17 the range of offsets over which the footprint of dominant arrivals such as reflection from the backstop, the intracrustal reflectors IR and IR′ and the Moho should be observed. The fit of both amplitude and phase of these arrivals was clearly improved between iterations 1 and 20.

[69] The time domain synthetic seismograms computed for OBS 17 are less convincing because they are polluted by a strong coda that overlaps the coherent secondary arrivals (Figure 18). The coda may have been partially generated by the model artifacts located near the landward end of the model. This is supported by the fact that the coda seems weaker in the synthetics computed for the 3 other modeled OBSs, farther seaward (Figures 18b–18d). The synthetics reasonably reproduce the overall pattern of the shallow refracted and reflected waves from the forearc basin deposits and the Shimanto wedge (Figure 18a) as well as the attenuation of the first arrival at offsets greater than 30 km. The reflection from the intracrustal reflector IR′ and from the Moho is visible in the synthetics although the computed amplitudes are lower than the observed ones, which is consistent with the partial fit of amplitudes observed in the frequency domain (Figure 14a). The weaker amplitudes of the Pn wave between offsets 60 and 80 km are qualitatively reproduced; the same goes for the higher amplitudes

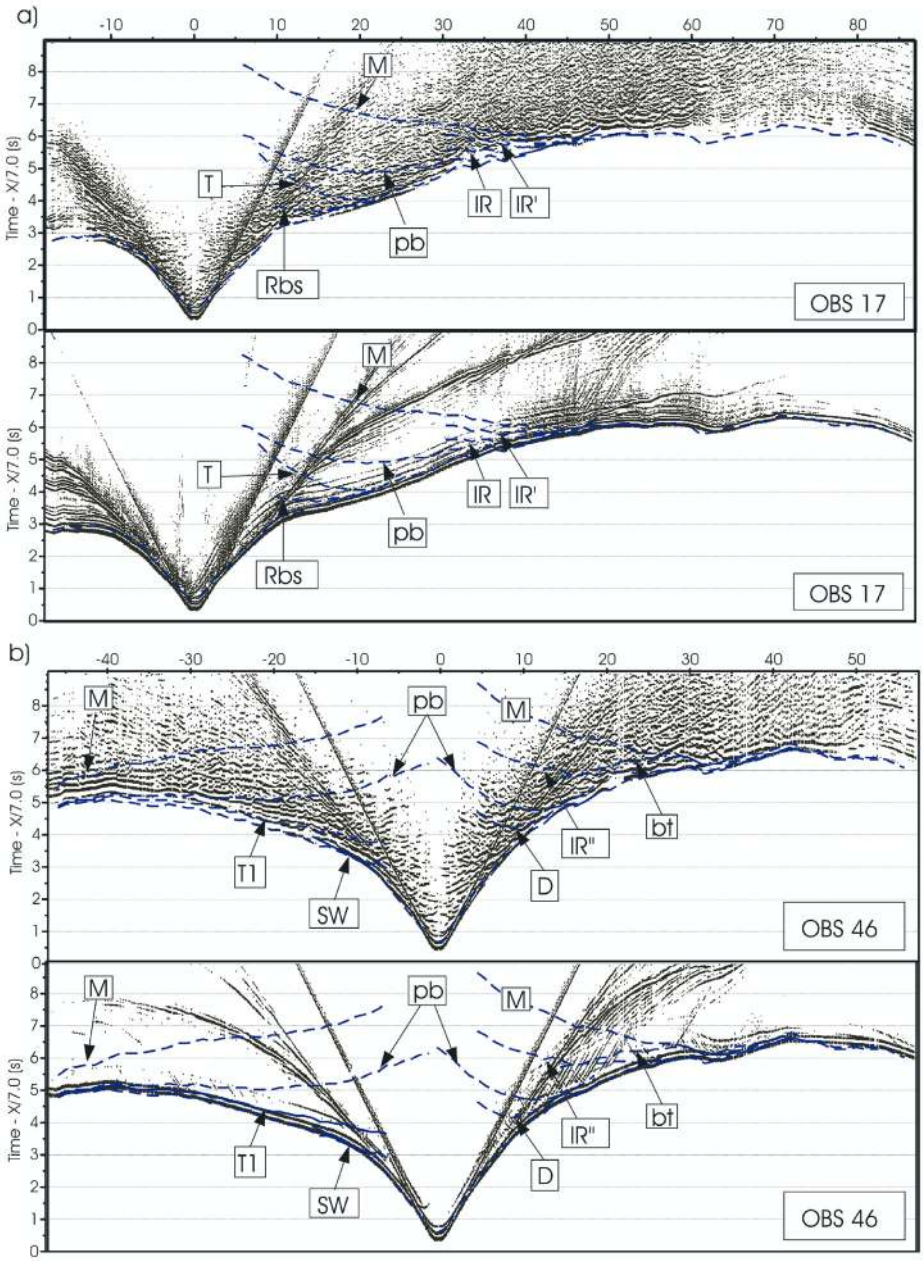

Figure 18. Time domain synthetic seismograms computed in the final FWT (top) and the FATT (bottom) models. The traveltime curves of Figure 16 are superimposed on the seismograms. (a) OBS 17; (b) OBS 46; (c) OBS 57; and (d) OBS 80.

at offsets greater than 80 km (Figures 4 and 18a). All these features that were partially modeled in the FWT synthetics are totally absent in the synthetics computed in the smooth FATT model (lower panel in Figure 18a) which exhibit a rather uniform amplitude versus offset behavior of the first arrival. We were unable to identify the phases Rbs and T in the synthetics of Figure 18a. We believe that they are properly modeled but are overprinted by the coda. This is supported by the good fit obtained in the frequency domain at offsets over which phases Rbs and T are observed (Figure 17a). These arrivals were also better modeled in the time domain synthetics computed in FWT models using only 10 iterations per frequency (not shown here). These 10-iteration models are less noisy than the 20-iteration ones but yield a degraded amplitude fit.

3.4.3.2. Modeling of OBS46

[70] For negative offsets, two main refracted arrivals are observed between offsets −3 and −10 km and between −10 and −30 km. These two refracted arrivals propagated in the forearc basin deposits and in the upper part of the Shimanto wedge (Figures 13a and 16b). The second refraction wave seems to undergo a sharp attenuation at offsets greater than 25 km, suggesting again a significant decrease of the vertical velocity gradient below ∼5 km depth. A wide-angle

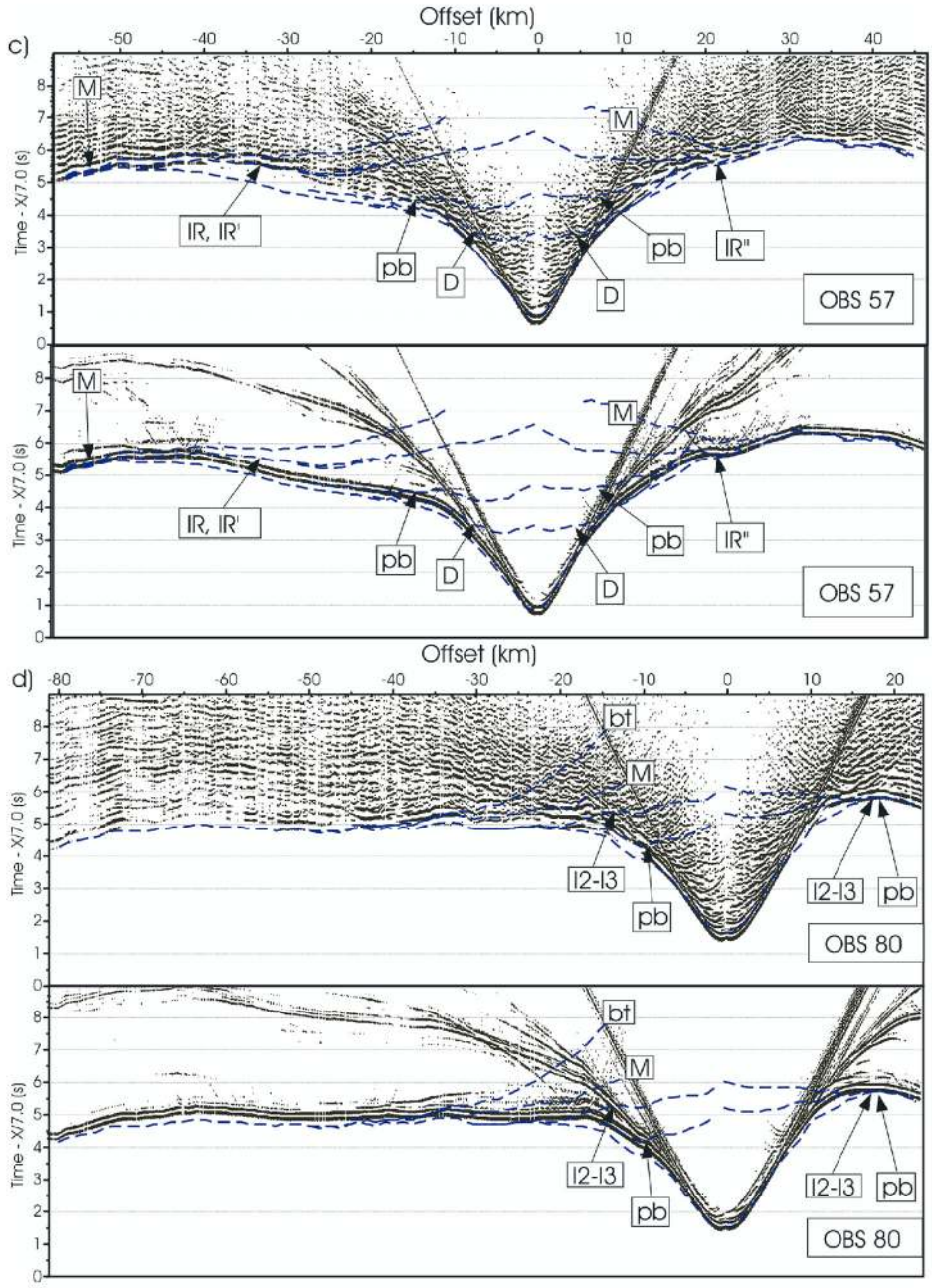

Figure 18. (continued)

reflected phase labeled T1 in Figure 4b is observed between offsets −25 and −4 km and interpreted as a reflection from the thrust T1 (Figures 13c and 16b). The PmP wave is observed between offsets −40 and −48 km as shown by the traveltime modeling (Figures 13e and 16b). At wide angle, the computed reflection from the plate boundary (PB) is very close in time to the reflection from the thrust (T1), since the latter is rooted on it. This can be checked by comparing the ray paths for the R1 and PB reflectors in Figures 13c and 13d and the PB and T1 traveltime curves merging at offsets greater than 40 km in Figure 16b. Therefore we conclude that the observed traveltimes of the plate boundary reflection are also fitted at offsets between −35 and −48 km, although this arrival cannot be distinguished from that reflected on T1 (Figure 16b). For positive offsets, rather complex arrivals are observed. We successfully modeled the traveltimes of four reflections, namely on the décollement (D), on the portion of the plate boundary corresponding to the landward flank of the Paleo-Zenisu ridge, on an intracrustal reflector (IR″) located at the base of the Paleo-Zenisu body, and on the Moho (Figures 13b–13e). Five interpretable refracted waves are also observed at these offsets; the first two, between ∼3 and 10 km offset, propagated above the décollement D. The

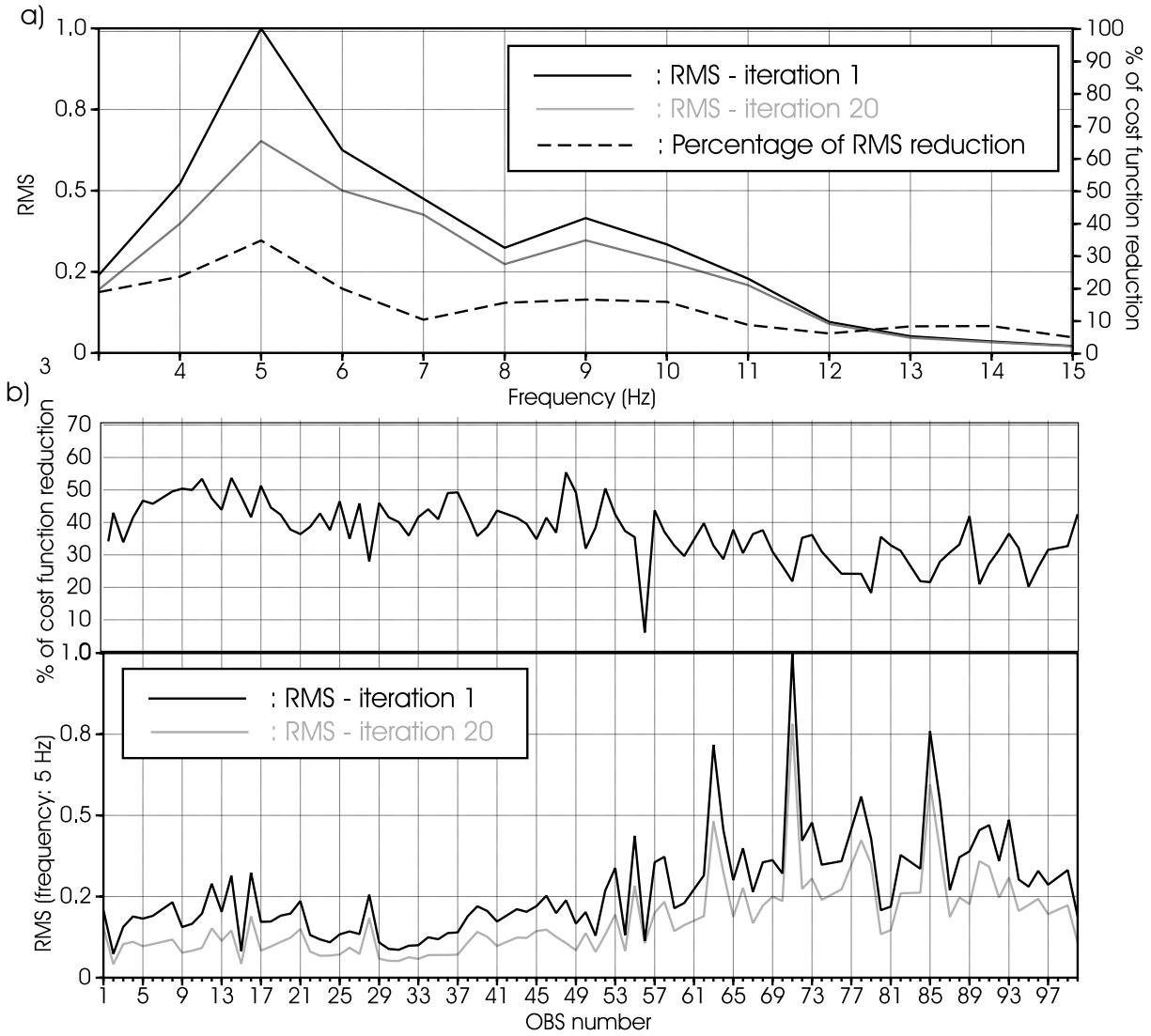

Figure 19. (a) Drop of the cost function plotted as a function of frequency (black line, iteration 1; gray line, iteration 20). Dashed line is percentage of reduction. The cost function curves are normalized with respect to the maximum observed at 5 Hz, iteration 1. They are obtained by summing over the full trace range. (b) (top) Percentage of cost function drop for each OBS gather for the dominant frequency (5 Hz). (bottom) Cost function at iteration 1 (gray line) and iteration 20 (dark line). The cost function curve is normalized with respect to its maximum (amplitude of the data are in arbitrary unit), and only its decrease is meaningful.

third propagated in the layer bounded by the décollement D and the top of the Paleo-Zenisu ridge (PB). The fourth is a very subtle phase refracted in the subducting oceanic crust, including the Paleo-Zenisu body, observed between offsets ~27 and 43 km and connecting the two wide-angle reflection phases IR″ and M. The fifth is the Pn wave observed at offsets greater than 43 km (Figures 13a and 16). Again, this phase identification was carried out by correlating the range of distance over which computed refracted rays in a given layer reach the surface and the range of offsets over which a refracted wave is observed in an OBS gather as a first arrival.

[71] The 5-Hz data fit is shown for the OBS 48 for which the higher cost function reduction was obtained (Figure 17b). The traveltime modeling described above was performed for the OBS 46 because this OBS was considered to exhibit the most comprehensive arrivals among the instruments located in the middle part of the profile. A cost function reduction of 40% and 55% was obtained at 5 Hz for OBSs 46 and 48, respectively. The fit of the 5-Hz frequency is excellent, both in terms of amplitude and phase except for the arrival located at offset 23 km whose amplitude is severely underestimated (Figure 17b).

[72] The time domain synthetics computed for the OBS 46 reproduce the overall pattern of arrivals T1, PB and M although the short-offset part of the arrival T1 seems to be affected by noise. The fit in the positive offsets is less convincing. We note though that the high amplitudes of the

PmP wave are well reproduced between offsets 35 and 48 km, followed by the smaller amplitudes of the Pn wave. Although waveforms of the computed wide-angle reflections are not optimally focused, we noticed the excellent match between observed and computed refraction and reflection traveltimes, suggesting that the reflected waves were sufficiently matched to provide an interpretable image of the reflectors.

3.4.3.3. Modeling of OBS57

[73] Two refracted phases are observed at negative offsets. The first one propagates above the reflector D while the second one propagates in the upper part of the backstop, above the reflector Rbs. The second refraction is strongly attenuated at offsets greater than 30 km as rays begin to propagate in the lower part of the backstop (below the Rbs reflector) and in the subducting oceanic crust (Figure 14a). A sharp wide-angle reflected arrival is observed between offsets −28 and −58 km and corresponds to a reflection on the intracrustal reflectors IR and IR′ (Figures 14d and 16c). The refraction ray paths allow delineation of the plate boundary from 18 to 38 km of distance (Figure 14a). These rays reach the surface between 0 and 10 km of distance, which corresponds to offsets ranging between −58 and −48 km. We did not observe clear first-arrival refraction in the data at these offsets, suggesting again a small velocity gradient at the base of the backstop and in the subducting oceanic crust. Combining subhorizontal ray paths refracted on top of the subducting oceanic crust for OBSs 17 and 57 allows characterization of the plate boundary between distances of 18 and 50 km; this latter distance marks the contact between the backstop and the Paleo-Zenisu ridge. At wide angle, the PmP traveltime-offset curve merges with that of the landward dipping IR′ reflector (Figures 14d, 14e, and 16c). The interference between the two arrivals is possibly indicated by a longer wavelet of the wide-angle reflection observed between offsets −53 and −58 km (Figures 4c and 16c). For positive offsets, reflections from the décollement D, the base of the Paleo-Zenisu body (IR″) and from the Moho are observed similarly to OBS 46 (Figure 16c). The reflection from the top of the Paleo-Zenisu ridge is not apparent in this OBS gather. Again the traveltimes of both refracted and reflected waves match the observations rather well (Figure 16c) validating the agreement between structures and observed phases.

[74] A cost function decrease of 44% was reached at 5 Hz for OBS 57 (Figure 19b). The signature of the strong wide-angle reflections from the intracrustal IR and IR′ and from the Moho is clearly visible in the 5-Hz data set, between offsets −30 and −58 km (Figure 17c). The fit of these arrivals was significantly improved both in terms of amplitude and phase from iteration 1 to 20. The fit of the reflection on IR″ was also been significantly improved for positive offsets, between 15 and 30 km.

[75] At negative offsets, the time domain synthetic seismograms computed in the FWT model exhibit the sharp wide-angle reflections from IR, IR′ and the Moho as well as the small amplitudes of the refracted waves in the accretionary wedge and the subducting oceanic crust (Figure 18c). Both features are not observed in the synthetics computed in the smooth traveltime tomography model. At positive offsets, the synthetics are polluted by a rather complex coda which makes the identification of subtle deterministic phases difficult; for example, reflections from the base of PZ and from the Moho whose amplitudes in the observed data are small. However, some features are reasonably reproduced such as the sedimentary arrival above the décollement D, the reflection from the décollement and the quickly attenuating refractions from below it, observed between offsets ∼15 and 20 km.

3.4.3.4. Modeling of OBS80

[76] The data exhibit mainly refracted arrivals from within the subducting oceanic crust and from the upper mantle (Figure 4d). Two wide-angle reflections from the layer 2/layer 3 interface and from the Moho are labeled l2–l3 and M in Figures 4d and 16d, respectively. The traveltime fit of both refracted and reflected phases is excellent (Figure 16d). The layer 2/layer 3 interface corresponds to a positive velocity jump between 5.5 and 6.5 km s^{-1} (Figure 11k) which is consistent with classical observations in oceanic crusts. The refraction ray paths allow delineation of the Moho between distances ∼40 and 65 km. One can note that refracted rays suddenly branch out at a distance of 60 km corresponding to the lower end of the landward dipping crustal thrust CT (Figure 15a). Landward of it, a low-velocity lens is observed around which the refracted ray beam splits out, the lower branch being propagated in the deeper part of the upper mantle. We interpret this zone as a patch of serpentinized mantle likely resulting from an alteration of peridotites by fluids channelled to depth along the adjacent crustal thrust. This is also illustrated in Figure 11f where velocities decrease from 7.5 km s^{-1} at the base of the crust to 7 km s^{-1}. Assembling the reverse refraction ray paths computed for OBSs 17 and 80 yields a geometry of the Moho between ∼25 and 90 km of distances.

[77] The cost function reduction for OBS80 is 35% (Figure 19b). The fit of the 5 Hz frequency is shown in Figure 17d where the footprint of the l2–l3 reflection and the PmP are interpretable. The time domain synthetic seismograms reproduce the amplitude highs associated with the l2–l3 and the PMP reflections between offsets −35 and −45 km and between offsets −15 and −25 km, respectively (Figure 18d).

4. Discussion: Resolution and Error Analysis

4.1. Resolution Analysis

[78] In this section, we tentatively quantify the spatial resolution of the FWT models and compare it with that predicted by the sensitivity kernel of FWT (Figure 2) and with that of the FATT models. We limit the resolution analysis to structures located at depths greater than 5 km for which a fold greater than 1 can be reasonably expected. Crustal structures can be decomposed into stochastic and deterministic components [e.g., *Holliger et al.*, 1993; *Brittan and Warner*, 1997]. The deterministic components are boundaries between the main structural units. We focus on these. No attempt is made to test whether some inference about the stochastic components of the crust can be proposed from FWT, since these features are by definition difficult if not impossible to interpret soundly.

[79] The qualitative examination of the perturbation models already revealed that the dominant wavelengths of the perturbation models typically range between 1 and 5 km (Figures 8, 9a, and 10). This estimation is supported by the

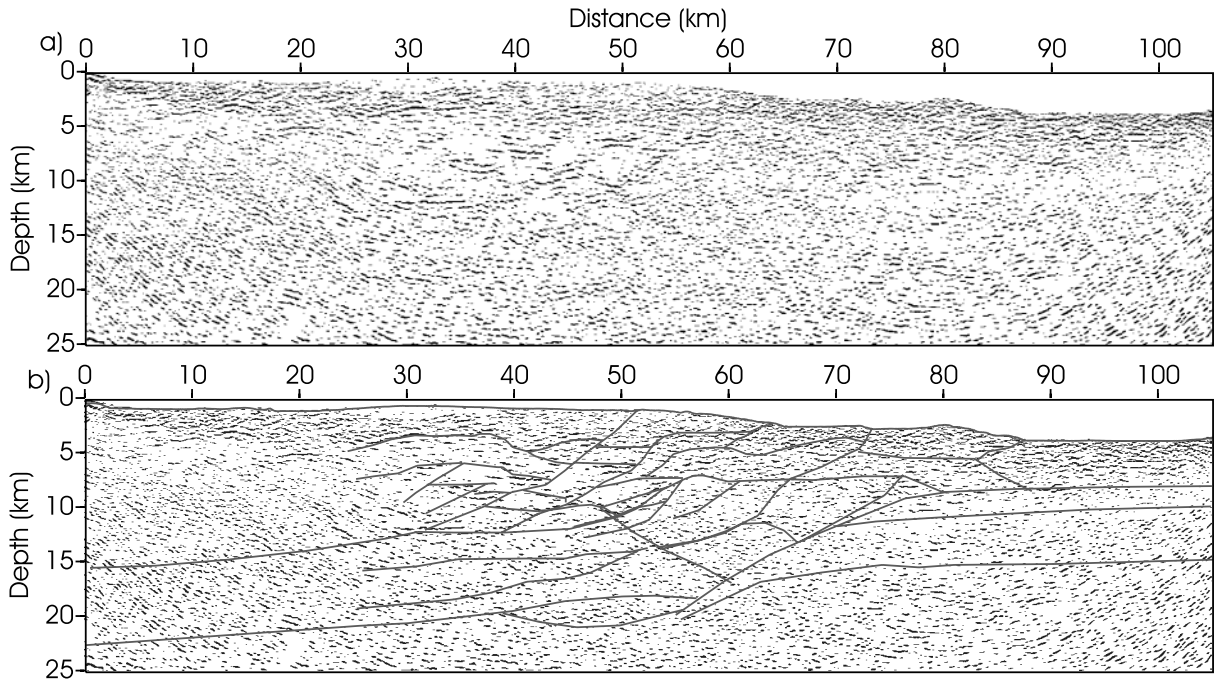

Figure 20. (a) The 15-Hz perturbation model after high-pass vertical wave number filter. The cutoff wave number is 0.0015 m-1. (b) Same with superimposed structural interpretation.

spectral amplitudes of a vertical profile extracted close to the center of the 15-Hz perturbation model (Figure 9c). The theoretical vertical resolution of FWT can be roughly estimated by considering some parameters representative of the experiment: for a depth of 10 km, an offset of 30 km and an average velocity of 5 km s^{-1}, the vertical resolution is assessed to be about 1.5–3.5, 0.9–2.1, and 0.3–0.7 km at 3, 5, and 15 Hz, respectively. The first bracketed values are inferred from (11) and provide a upper bound of the true theoretical resolution (i.e., a lower bound for reconstructed wavelengths) since they were obtained by considering a homogeneous velocity model which leads to a significant underestimation of the diffraction angle θ and thus to an overestimation in terms of wave numbers. The upper values of the intervals above were obtained by artificially augmenting the diffraction angle θ by 40 degrees to account for the curvature of the rays resulting from the overall increase of velocity with depth. The values for 3 and 5 Hz typically match the dominant wavelengths (1–5 km) observed in the perturbation models at 10-km depth, which suggests that these frequencies had a dominant contribution in the reconstruction of the velocity model. At 15 Hz, the resolution is higher than the characteristic scale of the layering.

[80] We now assess the real contribution of the frequencies well above 5 Hz in the model building. The vertical profile in Figure 9b shows that structures of dimension lower than 0.5 km are superimposed on the dominant wavelengths. A high-pass vertical wave number filter was applied to the final velocity model to estimate the lateral coherency of wavelengths below 600 m (Figure 20). The corresponding cutoff wave number is 0.0015 m^{-1}. The only coherent reflectors that can be identified deeper than ~2.5 km lie along the boundaries between the dominant wavelengths suggesting that these boundaries were sharpened by inverting frequencies up to 15 Hz. This sharpening is clearly visible in Figure 9b where the vertical profiles after the inversion of the 5 and 15 Hz components are superimposed. However, we acknowledge that inversion of frequencies significantly greater than 5 Hz did not characterize a layering thinner than that already imaged at 5 Hz.

[81] These conclusions raise the following question: what is the real characteristic scale of the layering in the deep crust of subduction zones? In other words, should we expect to observe structures of characteristic scale smaller than 1 km at depths between 5 and 15 km? Unfortunately, it is difficult to answer this question due to our limited knowledge of oceanic crustal structures at these levels of resolution ($\lambda < 1$ km) and at these depths (≥ 5 km).

[82] The vertical perturbation profiles and their spectral amplitudes also reveal that FWT weakly modified the very long wavelengths of the model, i.e., typically, those larger than 8 km (Figure 9c) in spite of the fact that any frequency is theoretically sensitive to these features when wide apertures are considered [*Pratt and Worthington*, 1990]. These long wavelengths are typically those that were constrained by FATT, as shown by a checkerboard test analysis [*Dessa et al.*, 2004a]: structures whose characteristic scale is 5 km were retrieved down to 10-km depth, whereas only 10-km structures were reconstructed between 10 and 15 km depth. Had long-wavelength components been significantly modified by FWT, first-arrival traveltimes computed in the FWT models would have been changed accordingly. This would have violated the key assumption imposed by the linearized formulation of the waveform inverse problem to ensure that cycle skipping is avoided. If this condition is not verified, erroneous velocity models will be obtained. The fact that the large wavelengths were not significantly perturbed suggests that the FATT model was accurate enough to

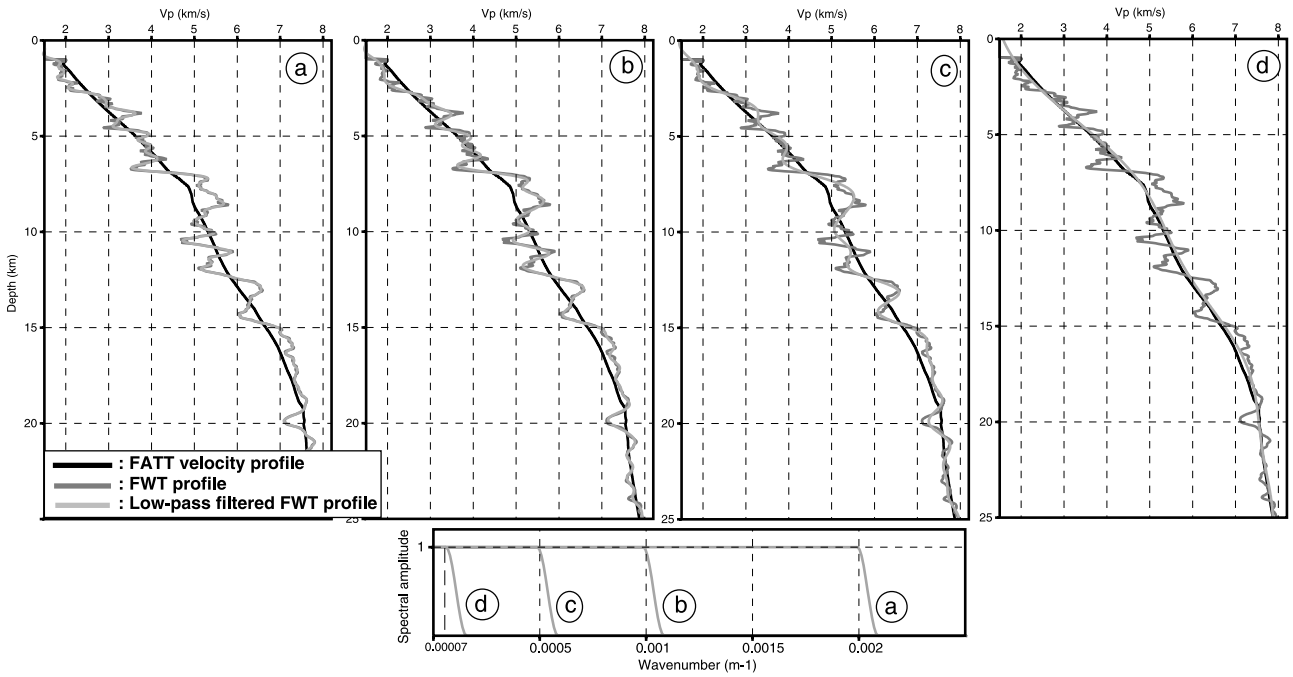

Figure 21. Illustration of the resolution gain provided by FWT with respect to FATT. The dark and light gray lines correspond the raw and low-pass-filtered FWT profiles, respectively. The black line is the vertical profile extracted from the FATT model. The spectral amplitude of the low-pass filters corresponding to each panel are shown on the bottom. See text for details.

prevent cycle skipping and hence that FWT did not degrade the kinematic accuracy of the reconstructed velocity models. This conclusion is supported by the fit between first-arrival traveltimes computed in the FWT models and the observed ones that was shown in section 3.

[83] The perturbation models remain stable over the successive single-frequency inversions. By stability, we mean that the interpreted structures remained coherent in spite of the fact that independent monochromatic data sets were successively introduced in the process (Figure 8). This argument makes us confident in the validity of our results.

[84] To quantify the resolution improvement provided by FWT with respect to FATT, we extracted a velocity profile from the final 15-Hz FWT model and its counterpart from the FATT model, at 50 km of distance, and applied a series of low-pass filter to the first one until it approximately fits the second (Figure 21). A rough agreement was obtained for a cutoff wave number of 0.00007 m^{-1}, which corresponds to a wavelength of 14 km. At the other extremity, a cut off wave number of 0.0015 m^{-1} begins to degrade the image of the discontinuities, suggesting that the maximum resolution of FWT is of the order of 500 m. We conclude that FWT improves the resolution of the imaging by over an order of magnitude with respect to FATT.

4.2. Error Analysis

[85] A rigorous estimation of the uncertainties that affect reconstructed velocities should follow the estimation of the best fitting model [*Scales and Snieder*, 2000; *Tarantola*, 1987; *Tichelaar and Ruff*, 1989]). However, this task is out of reach from a computational viewpoint when large data sets and multidimensional models are considered such as in this study. The more robust error analysis are based on Monte Carlo sampling methods such as the bootstrapping or jackknifing [i.e., *Tichelaar and Ruff*, 1989]. An intermediary approach is based on the analysis of the a posteriori model covariance matrix assuming a Gaussian probability distribution [e.g., *Tarantola*, 1987; *Gouveia and Scales*, 1998]. Estimation of the a posteriori covariance matrix requires to compute the inverse of the approximate Hessian $[\mathbf{A}^{\mathrm{T}} C_d \mathbf{A} + C_M^{-1}]$ which is computationally unpractical. Only the diagonal terms of the approximate Hessian are computed in our case (equation (8)). Apart from the computational aspect, the a posteriori covariance matrix provides useful insights on the errors in the output models only if realistic a priori estimates of the data and theory errors can be quantified in the data covariance matrix [*Sen and Stoffa*, 1995; *Gouveia and Scales*, 1998].

[86] In waveform inversion, the sources of errors are multiple and may be sorted into four main categories that are more extensively discussed hereafter: (1) those resulting from the approximation made in modeling the physics of wave propagation, in our case, a 2-D acoustic approximation; (2) those that can be linked to the experimental setup; (3) those arising from the noise in data; and (4) those related to the linearization of the inverse problem.

[87] Concerning the 2-D approximation, it is impossible to quantify the error in the velocity models resulting from this approximation. The reasonable fit of the first-arrival traveltimes validates the 2-D approximation that is used [*Dessa et al.*, 2004a]. It is also difficult to quantify the errors resulting from the acoustic approximation. They mainly

concern the estimation of the velocity contrasts at discontinuities since the partitioning of energy at interfaces is not properly taken into account. However, this approximation does not prevent a correct positioning of the main discontinuities in depth. If mode converted reflected waves are left in the data, probably a marginal effect since inverted data are the vertical components of OBSs, these waves are misinterpreted as P waves reflected from a dipping interface where the dip of the interface compensates for the discrepancy between P and S wave velocities. If we consider an homogeneous elastic half-space above a flat interface and a S wave reflection from this interface, then, the dip ϕ of the imaged interface resulting from the migration of the S wave reflection with a P wave velocity is given by

$$\cos\phi = \frac{V_S}{V_P} \tag{13}$$

As an illustrative example, a Poisson coefficient of 0.28 and a P wave velocity of 5 km s^{-1} give an S wave velocity of 2.76 km s^{-1} which leads to a dip of 56.5 degrees. The maximum dip that is observed in the velocity models is around 40 degrees suggesting that PS converted waves have a negligible impact in the reconstructed velocity structures. This is consistent with the fact that we were unable to identify coherent P-SV waves in the OBS gathers (Figure 4). An elastic description of the crust is obviously physically more accurate than an acoustic one. However, the implementation of elasticity in the crustal-scale inverse problem raises several difficult questions: the first one is related to the fact that PS converted waves are seldom observed in OBS data recorded in complex geological setup while theory would predict a significant amount of conversion. Among possible explanations, rugged interface may prevent the converted shear waves from being phase coherent [*White and Stephen*, 1980]. Unfortunately, characterizing the interface roughness is far beyond the resolution achievable here. The second question concerns the building of the starting S wave model by traveltime tomography. The picking of doubly converted waves in marine environment is most of the time far from obvious. This difficulty raises in turn the question of the sensitivity of FWT with respect to errors in the starting S wave models, which should theoretically verify the same criteria of accuracy than the P wave model to avoid cycle skipping.

[88] Regarding the experimental setup, the air gun shots are probably not perfectly reproducible and the seafloor coupling may vary from one receiver to the other. Moreover, the large spacing between OBSs leads to spatial aliasing in the shallow part of the velocity model. These errors in the subsurface are probably propagated deeper in the structure. One single source was estimated to fit the whole data set using (11), thereby assuming that each shot had the same signature and energy. We also tried to estimate a separate source for each OBS gather to account for possible variations in ground coupling but this led to degraded results. Using one single source for the full data set allowed us to match the amplitudes to a reasonable level (Figure 17) suggesting that the assumptions of single source and perfect coupling are reasonable here.

[89] The reduction of the cost function computed for each OBS gather at 5 Hz is reasonably uniform all over the receivers (except for OBS 56) showing that each OBS gather has a comparable contribution in the model reconstruction. We note however the reduction is slightly degraded when progressing oceanward in Figure 19b. We interpret this as the result of the mute window which is broader for OBS deployed in deeper sea environment (Figures 5a and 5b): the larger amount of information to fit makes the convergence more difficult to achieve. This trend is also correlated with a degradation of the signal-to-noise ratio of the velocity model toward the ocean (Figure 8).

[90] The curve showing the percentage of cost function reduction as a function of the inverted frequency exhibits a pattern comparable to that of the frequency spectrum of data (Figure 5c): each curve has local minima at frequencies 8 and 13 Hz. The lower reduction of the cost function at these frequencies is directly related to the lower signal-to-noise ratio affecting these spectral components.

[91] When talking about noise, we mean any fraction of the signal that is not predicted by the wave modeling tool. This includes incoherent energy noise as well as seismic arrivals that are not modeled, such as converted PS waves. No attempt was made to assign an a priori uncertainty to each trace that would depend of its specific signal-to-noise ratio. We have rather performed a quality control of the traces before inversion to remove those for which the ratio was unacceptably large.

[92] At last, the linearization of the inverse problem implies a local search of the minimum of the cost function in the vicinity of the starting velocity model. As for the error analysis, the sensitivity of a linearized inverse problem to the starting model should be assessed by Monte Carlo sampling methods which are computationally out of reach [*Korenaga et al.*, 2000]. As mentioned before, the fit between first-arrival traveltimes computed in the FWT models and the observed ones shows the robustness of FWT with respect to the starting model developed by FATT.

5. Conclusion

[93] We presented the first application of 2-D crustal-scale FWT to dense OBS data. This is a first attempt toward an exploitation of the full information content of global aperture seismic data recorded by dense arrays of OBSs. We inferred a series of velocity models of increasing resolution as the full waveform inversion was evolving toward higher frequencies. We provided a quantification of the spatial resolution of the velocity models that was compared with the theoretical resolution of FWT predicted by its sensitivity kernel. We demonstrated that the spatial resolution was improved by an order of magnitude with respect to that provided by FATT, at least in the central part of the model which benefits from an optimal wavefield coverage. The estimation of the best fitting model was followed, first, by a structural interpretation and, subsequently, by probing and appraising the velocity model. The structural interpretation was performed by delineating short-wavelength structures revealed by the perturbation models and by verifying the consistency between the interpretation of these boundaries with the possible lithologies of the structural units they separate, as revealed by the values of the absolute P wave velocities. In some cases, we also introduced geological

likelihood to draw some pieces of subtle reflectors associated with weak velocity contrasts.

[94] The relevance of the interpreted structures were verified by ray tracing and time and frequency domain FD synthetic seismogram modeling. This practical appraisal phase was proposed in substitution to more quantitative approaches based on Monte Carlo sampling methods or analysis of a posteriori model covariance matrices, these somewhat more rigorous approaches happening to be completely unpractical due to the computational cost of the multidimensional forward and inverse problems their completion requires. Apart from these numerical limitations, it remains fairly difficult to rigorously account for all sources of error in the a priori data and model covariance matrices.

[95] The best fitting model allowed us to image major structures controlling the tectonic regime of the eastern subduction zone. Among these structures are the subducting Paleo-Zenisu ridge which is shown to be presently adjacent to the rigid backstop and on top of which lies the décollement. Intense compressive regime was evidenced by several thrust faults, both in the backstop and the subducting oceanic crust. The Moho was clearly imaged all along the profile. A lens of partially serpentinized mantle below a crustal-scale thrust affecting the subducting oceanic crust is proposed. Prolongation in depth of major thrusts was imaged, such as the Kodaiba fault which is revealed to be rooted on the plate boundary, thus confirming that it may play a major role during the rupture propagation of the large megathrust earthquakes, one of which often referred to as the Tokai earthquake being expected in the next decades.

[96] Several intracrustal reflectors were also imaged in the subducting oceanic crust and their relevance was confirmed by the modeling of their strong seismic response identified in the data. The geological interpretation of these structures and the role they may play in the seismicity of this subduction system still requires further geological expertise. An insight of their lateral prolongation is required in particular.

[97] Application of FWT requires to develop important acquisition systems involving voluminous OBS arrays and to dedicate global aperture seismic experiment to relatively focused targets. We hope that the results presented in this paper will stimulate the buildup of such multifold global aperture seismic experiments in the near future. We are unable yet to provide some general rules to define the minimum OBS spacing required to avoid spatial aliasing. The fold of crustal-scale OBS experiment depends on the offset range over which a specific reflection is observed. This offset range depends in turn of several parameters such as the reflector depth, the signal-to-noise ratio, the lateral heterogeneity and the structure of the reflector. It is clear that any decrease of the OBS spacing will allow increase of the fold and hence the signal-to-noise ratio of the tomography models. An optimal trade-off between the length of the OBS array required to record refracted waves in the deepest targeted structure and its spatial sampling has to be found, keeping in mind that the dominant criterion must be a sufficient length of profile to ensure that deeply refracted phases are recorded, which is crucial to derive a robust kinematic model and to linearize the full waveform inverse problem.

[98] A full exploitation of the data and a more significant quantitative analysis of velocities will require improvement of the tomography approach presented in this paper. In the 2-D approximation, improvements concern incorporation of more subtle wave propagation effects such as anisotropy and viscoelasticity. The sensitivity of seismic amplitudes to intrinsic attenuation in a rather low-frequency range (3–20 Hz) must be assessed. Attenuation can be implemented easily in the frequency domain wave propagation modeling by using complex-valued velocities. Hence the inverse problem may be implemented in a rather straightforward way, provided that a suitable attenuation model is available.

[99] Accounting for P-to-S wave conversion should theoretically be required when considering wide-aperture reflections for which theory predicts significant mode conversions at interfaces. However, the interpretation of converted arrivals and their traveltime picking is rarely obvious, especially in the case of complex structures with rugged interfaces. The construction of a reliable and accurate S wave velocity starting model by P-to-S wave traveltime tomography will probably be a major obstacle to the application of elastic full waveform tomography to such complex structures. Implementation of elasticity in both the forward and inverse problems will also lead to a significant increase of the computational cost of the method, first because two wavefields, vertical and horizontal particle velocities, and two data components, vertical and horizontal, will need to be accounted for and because a suitable elastic stencil accounting for the fluid-solid and the free surface-solid interfaces will require a finer spatial discretization than in the acoustic case [*Jo et al.*, 1996; *Stekl and Pratt*, 1998; *Gélis et al.*, 2005].

[100] For all these reasons, we believe that the most logical and reasonable approach was to start by investigating acoustic full waveform tomography applied to crustal-scale problems, living with all the associated approximations, and to objectively assess the improvements that could be expected by accounting for more subtle wave propagation effects in a forthcoming step.

Appendix A: Fitting Observed Vertical Geophone Data With Pressure Synthetics

[101] We establish here the spatial reciprocity relationship between vertical particle velocity wavefields generated by explosions and pressure wavefields generated by a vertical force.

[102] We first express the spatial reciprocity of Green functions in terms of particle velocity in the four following cases

$$\begin{aligned} v_{x^+}^{z^+}(s_x+h,s_z,t;r_x,r_z,0) &= v_{z^+}^{x^+}(r_x,r_z,t;s_x+h,s_z,0)\\ v_{x^-}^{z^+}(s_x-h,s_z,t;r_x,r_z,0) &= v_{z^+}^{x^-}(r_x,r_z,t;s_x-h,s_z,0)\\ v_{z^+}^{z^+}(s_x,s_z+h,t;r_x,r_z,0) &= v_{z^+}^{z^+}(r_x,r_z,t;s_x,s_z+h,0)\\ v_{z^-}^{z^+}(s_x,s_z-h,t;r_x,r_z,0) &= v_{z^+}^{z^-}(r_x,r_z,t;s_x,s_z-h,0) \end{aligned} \tag{A1}$$

where the superscript denotes the force direction and the subscript denotes the direction of the particle velocity. The sign ± assigned to the force direction indicates whether the vertical and horizontal forces point upward or downward and leftward or rightward, respectively. The $(s_x,\ s_z)$ and $(r_x,\ r_z)$ are the coordinates of source and

receiver positions. The grid step h is assumed to be a small shift applied to the spatial coordinates here.

[103] Exploiting the fact that $v_{x+} = -v_{x^-}$ and $v_{z+} = -v_{z^-}$ and using the convention $x \equiv x^+$, $z \equiv z^+$, the above equations can be written more compactly as

$$\begin{aligned} v_x^z(s_x + h, s_z, t; r_x, r_z, 0) &= v_z^{x^+}(r_x, r_z, t; s_x + h, s_z, 0) \\ -v_x^z(s_x - h, s_z, t; r_x, r_z, 0) &= v_z^{x^-}(r_x, r_z, t; s_x - h, s_z, 0) \\ v_z^z(s_x, s_z + h, t; r_x, r_z, 0) &= v_z^{z^+}(r_x, r_z, t; s_x, s_z + h, 0) \\ -v_z^z(s_x, s_z - h, t; r_x, r_z, 0) &= v_z^{z^-}(r_x, r_z, t; s_x, s_z - h, 0). \end{aligned} \tag{A2}$$

By summing these four equations, we obtain

$$\begin{aligned} 2h \left(\frac{\partial v_x^z(r_x, r_z, t; s_x, s_z, 0)}{\partial x} + \frac{\partial v_z^z(r_x, r_z, t; s_x, s_z, 0)}{\partial z} \right) \\ = v_z^{\Delta p}(r_x, r_z, t; s_x, s_z, 0) \end{aligned} \tag{A3}$$

where the superscript Δp denotes an explosive pressure source which is equivalent to two perpendicular vector dipoles with an applied arm of $2h$.

[104] In the left-hand side term of (3), we used the following FD approximation

$$\begin{aligned} &\frac{\partial v_x^z(r_x, r_z, t; s_x, s_z, 0)}{\partial x} \\ &\approx \frac{v_x^z(s_x + h, s_z, t; r_x, r_z, 0) - v_x^z(s_x - h, s_z, t; r_x, r_z, 0)}{2h} \\ &\cdot \frac{\partial v_z^z(r_x, r_z, t; s_x, s_z, 0)}{\partial z} \\ &\approx \frac{v_x^z(s_x, s_z + h, t; r_x, r_z, 0) - v_x^z(s_x, s_z - h, t; r_x, r_z, 0)}{2h} \end{aligned} \tag{A4}$$

Exploiting Hooke's law, we can express the left-hand side term of equation (3) as a function of pressure

$$\frac{2h}{K} \frac{\partial P^z(r_x, r_z, t; s_x, s_z, 0)}{\partial t} = v_z^{\Delta p}(r_x, r_z, t; s_x, s_z, 0) \tag{A5}$$

Equation (5) shows that in the acoustic case, one can match a pressure wavefield generated by a vertical force with a vertical velocity wavefield generated by an explosion.

[105] If the shot position is denoted by s and the OBS position by r, equation (5) indicates that one can match the data arising from an explosive source and recorded on the vertical geophone of an OBS with pressure synthetics recorded at the shot position and emitted by a vertical force located at the OBS position, provided that no shear waves are propagated.

[106] This reciprocity relationship still applies when the Green functions are convolved with a source term (the convolution is linear), which makes it applicable to field data.

[107] **Acknowledgments.** We thank the scientific and technical boarding crew of the R/V *Kayio* in charge of data acquisition (chief scientist, A. Nakanishi). We thank S. Kodaira (JAMSTEC) for providing the data and for fruitful discussions. We thank an anonymous reviewer, A. Trehu, and D. Toomey (Associate Editor) for their constructive comments and for the time spent for reviewing the manuscript. We are very grateful to P. Amestoy and J. Y. L'Excellent for providing us the MUMPS software (parallel multifrontal LU solver) and for their assistance. This paper is dedicated to the memory of G. Pascal.

References

Amestoy, P. R., I. S. Duff, and J. Y. L'Excellent (2000), Multifrontal parallel distributed symmetric and unsymmetric solvers, *Comput. Methods Appl. Mech. Eng.*, *184*, 501–520.

Amestoy, P. R., I. S. Duff, J. Koster, and J. Y. L'Excellent (2001), A fully asynchronous multifrontal solver using distributed dynamic scheduling, *SIAM J. Matrix Anal. Appl.*, *23*(1), 15–41.

Ando, M. (1975a), Possibility of a major earthquake in the Tokai district, Japan and its pre-estimated seismotectonic effects, *Tectonophysics*, *27*, 69–85.

Ando, M. (1975b), Source mechanisms and tectonic significance of historical earthquakes along the Nankai trough, Japan, *Tectonophysics*, *27*, 119–140.

Brittan, J., and M. Warner (1997), Wide-angle seismic velocities in heterogeneous crust, *Geophys. J. Int.*, *129*, 269–280.

Cannat, M. (1996), How thick is the magmatic crust at slow spreading oceanic ridges?, *J. Geophys. Res.*, *101*(B2), 2847–2858.

Crase, E., A. Pica, M. Noble, M. Donald, and A. Tarantola (1990), Robust elastic non-linear waveform inversion: Application to real data, *Geophysics*, *55*, 527–538.

Crase, E., C. Wideman, M. Noble, and A. Tarantola (1992), Nonlinear elastic inversion of land seismic reflection data, *J. Geophys. Res.*, *97*, 4685–4705.

Cummins, P. R., T. Baba, S. Kodaira, and Y. Kaneda (2002), The 1946 Nankai earthquake and segmentation of the Nankai trough, *Phys. Earth Planet. Inter.*, *132*, 75–87.

Dessa, J.-X., S. Operto, S. Kodaira, A. Nakanishi, G. Pascal, K. Uhira, and Y. Kaneda (2004a), Deep seismic imaging of the eastern Nankai trough, Japan, from multifold ocean bottom seismometer data by combined travel time tomography and prestack depth migration, *J. Geophys. Res.*, *109*, B02111, doi:10.1029/2003JB002689.

Dessa, J.-X., S. Operto, S. Kodaira, A. Nakanishi, G. Pascal, J. Virieux, and Y. Kaneda (2004b), Multiscale seismic imaging of the eastern Nankai trough by full waveform inversion, *Geophys. Res. Lett.*, *31*, L18606, doi:10.1029/2004GL020453.

Devaney, A. J. (1982), A filtered back propagation algorithm for diffraction tomography, *Ultrasonic Imaging*, *4*, 336–350.

Gauthier, O., J. Virieux, and A. Tarantola (1986), Two-dimensional nonlinear inversion of seismic waveforms: Numerical results, *Geophysics*, *51*(7), 1387–1403.

Gélis, C., D. Leparoux, J. Virieux, A. Bitri, S. Operto, and G. Grandjean (2005), Numerical modelling of surface waves over shallow cavities, *J. Environ. Eng. Geophys.*, *10*(2), 111–122.

Gouveia, W. P., and J. A. Scales (1998), Bayesian seismic waveform inversion: Parameter estimation and uncertainty analysis, *J. Geophys. Res.*, *103*(B2), 2579–2779.

Hobro, J. W. D., S. C. Singh, and T. A. Minshull (2003), Three-dimensional tomographic inversion of combined reflection and refraction seismic traveltime data, *Geophys. J. Int.*, *152*, 79–93.

Holliger, K., A. R. Levander, and J. A. Goff (1993), Stochastic modeling of the reflective lower crust: Petrophysical and geological evidence from the Ivrea zone (northern Italy, *J. Geophys. Res.*, *98*(B7), 11,967–11,980.

Hustedt, B., S. Operto, and J. Virieux (2004), Mixed-grid and staggered-grid finite difference methods for frequency-domain acoustic wave modelling, *Geophys. J. Int.*, *157*, 1269–1296.

Jo, C.-H., C. Shin, and J. H. Suh (1996), An optimal 9-point, finite-difference, frequency-space, 2-d scalar wave extrapolator, *Geophysics*, *61*(2), 529–537.

Kodaira, S., E. Kurashimo, J.-O. Park, N. Takahashi, A. Nakanishi, S. Miura, T. Iwasaki, N. Hirata, K. Ito, and Y. Kaneda (2002), Structural factors controlling the rupture process of a megathrust earthquake at the Nankai trough seismogenic zone, *Geophys. J. Int.*, *149*, 815–835.

Kodaira, S., A. Nakanishi, J. Park, A. Ito, T. Tsuru, and Y. Kaneda (2003), Cyclic ridge subduction at an inter-plate locked zone off central Japan, *Geophys. Res. Lett.*, *30*(6), 1339, doi:10.1029/2002GL016595.

Kodaira, S., T. Lidaka, A. Kato, J.-O. Park, T. Iwasaki, and Y. Kaneda (2004), High pore fluid pressure may cause silent slip in the Nankai trough, *Science*, *304*, 1295–1298.

Kolb, P., F. Collino, and P. Lailly (1986), Prestack inversion of 1-D medium, *Proc. Inst. Electr. Electron. Eng. Extended Abstr.*, *74*, 498–508.

Korenaga, J., W. S. Holbrook, G. M. Kent, P. B. Kelemen, R. S. Detrick, H.-C. Larsen, J. R. Hopper, and T. Dahl-Jensen (2000), Crustal structure of the southeast Greenland margin from joint refraction and reflection seismic tomography, *J. Geophys. Res.*, *105*(B9), 21,591–21,614.

Kumagai, K. (1996), Time sequence and the recurrence models for large earthquakes along the Nankai trough revisited, *Geophys. Res. Lett.*, *23*, 1139–1142.

Lailly, P. (1984), The seismic inverse problem as a sequence of before stack migrations, in *Conference on Inverse Scattering: Theory and Application*, edited by J. B. Bednar et al., pp. 206–220, Soc. for Ind. and Appl. Math., Philadelphia, Pa.

Lallemand, S., J. Mallavieille, and S. Calassou (1992), Effects of ridge oceanic subduction on accretionary wedges: Experimental modeling and marine observations, *Tectonics*, *11*, 1301–1313.

Lallemant, S., N. Chamot-Rooke, X. Le Pichon, and C. Rangin (1989), Zenisu ridge: A deep intraoceanic thrust related to subduction, off southwest Japan, *Tectonophysics*, *160*, 151–174.

Lambaré, G., S. Operto, P. Podvin, P. Thierry, and M. Noble (2003), 3-D ray+Born migration/inversion - part 1: Theory, *Geophysics*, *68*, 1348–1356.

Le Pichon, X., S. Lallemant, H. Tokuyama, F. Thoué, P. Huchon, and P. Henry (1996), Structure and evolution of the backstop in the eastern Nankai trough area (Japan): Implications for the soon-to-come Tokai earthquake, *Island Arc*, *5*, 440–454.

Martin, V. (2003), Structure et tectonique du prisme d'accrétion de Nankai dans la zone de Tokai par imagerie sismique en trois dimensions, Ph.D. thesis, Univ. de Paris Sud, Orsay, France.

Mazzotti, S., P. Henry, X. L. Pichon, and T. Sagiya (1999), Strain partitioning in the zone of transition from Nankai subduction to Izu-Bonin collision (central Japan): Implications for an extensional tear within the subducting slab, *Earth Planet. Sci. Lett.*, *172*, 1–10.

Mazzotti, S., S. Lallemant, P. Henry, X. L. Pichon, H. Tokuyama, and N. Takahashi (2002), Intraplate shortening and underthrusting of a large basement ridge in the eastern Nankai subduction zone, *Mar. Geol.*, *187*, 63–88.

Miller, D., M. Oristaglio, and G. Beylkin (1987), A new slant on seismic imaging: Migration and integral geometry, *Geophysics*, *52*(7), 943–964.

Mochizuki, K., et al. (2005), Intense PP reflection beneath the aseismic forearc slope of the Japan trench subduction zone and its implication of aseismic slip subduction, *J. Geophys. Res.*, *110*, B01302, doi:10.1029/2003JB002892.

Nakamura, Y., P. L. Donoho, P. H. Roper, and P. McPherson (1987), Large-offset seismic surveying ocean-bottom seismographs and air guns: Instrumentation and field technique, *Geophysics*, *52*, 1601–1611.

Nakanishi, A., H. Shiobara, R. Hino, S. Kodaira, T. Kanazawa, and H. Shinamura (1998), Detailed subduction structure across the eastern Nankai trough obtained from ocean bottom seismograph profiles, *J. Geophys. Res.*, *103*(B11), 27,151–27,168.

Operto, S., C. Ravaut, L. Improta, J. Virieux, A. Herrero, and P. Dell' Aversana (2004), Quantitative imaging of complex structures from dense wide-aperture seismic data by multiscale traveltime and waveform inversions: A case study, *Geophys. Prospect.*, *52*, 625–651.

Pica, A., J. P. Diet, and A. Tarantola (1990), Nonlinear inversion of seismic reflection data in laterally invariant medium, *Geophysics*, *55*, 284–292.

Podvin, P., and I. Lecomte (1991), Finite difference computation of traveltimes in very contrasted velocity model: A massively parallel approach and its associated tools, *Geophys. J. Int.*, *105*, 271–284.

Pratt, R. G. (1999), Seismic waveform inversion in the frequency domain, part 1: Theory and verification in a physical scale model, *Geophysics*, *64*, 888–901.

Pratt, R. G., and M. H. Worthington (1990), Inverse theory applied to multi-source cross-hole tomography. part 1: Acoustic wave-equation method, *Geophys. Prospect.*, *38*, 287–310.

Pratt, R. G., Z. Song, and M. Warner (1996), Two-dimensional velocity models from wide-angle seismic data by wavefield inversion, *Geophys. J. Int.*, *124*, 323–340.

Pratt, R. G., C. Shin, and G. J. Hicks (1998), Gauss-Newton and full Newton methods in frequency-space seismic waveform inversion, *Geophys. J. Int.*, *133*, 341–362.

Ravaut, C., S. Operto, L. Improta, J. Virieux, A. Herrero, and P. Dell' Aversana (2004), Multiscale imaging of complex structures from multi-fold wide-aperture seismic data by frequency-domain full-waveform tomography: Application to a thrust belt, *Geophys. J. Int.*, *159*, 1032–1056.

Scales, J. A., and R. Snieder (2000), The anatomy of inverse problems, *Geophysics*, *65*, 1708–1710.

Sen, M., and P. Stoffa (1995), *Global Optimization Methods in Geophysical Inversion*, Elsevier, New York.

Seno, T., S. Stein, and A. E. Gripp (1993), A model for the motion of the Philippine Sea plate consistent with NUVEL-1 and geologic data, *J. Geophys. Res.*, *98*, 17,941–17,948.

Shin, C., K. Yoon, K. J. Marfurt, K. Park, D. Yang, H. Y. Lim, S. Chung, and S. Shin (2001), Efficient calculation of a partial derivative wavefield using reciprocity for seismic imaging and inversion, *Geophysics*, *66*, 1856–1863.

Shinohara, M., K. Suyehiro, S. Matsuda, and K. Ozawa (1993), Digital recording of ocean bottom seismometer using portable digital audio tape recorder, *J. Jpn. Soc. Mar. Surv. Technol.*, *5*, 21–31.

Shipp, R. M., and S. C. Singh (2002), Two-dimensional full wavefield inversion of wide-aperture marine seismic streamer data, *Geophys. J. Int.*, *151*, 325–344.

Sirgue, L., and R. G. Pratt (2004), Efficient waveform inversion and imaging: A strategy for selecting temporal frequencies, *Geophysics*, *69*, 231–248.

Stekl, I., and R. G. Pratt (1998), Accurate viscoelastic modeling by frequency-domain finite differences using rotated operators, *Geophysics*, *63*, 1779–1794.

Tarantola, A. (1984), Inversion of seismic reflexion data in the acoustic approximation, *Geophysics*, *49*, 1259–1266.

Tarantola, A. (1987), *Inverse Problem Theory: Methods for Data Fitting and Model Parameter Estimation*, Elsevier, New York.

Tichelaar, B. W., and L. R. Ruff (1989), How good are our best models?, *Eos Trans. AGU*, *70*, 593, 605–606.

Toksoz, M., and D. Johnston (1981), *Seismic Wave Attenuation*, Soc. of Explor. Geophys., Tulsa, Okla.

Toomey, D. R., S. C. Solomon, and G. M. Purdy (1994), Tomographic imaging of the shallow crustal structure of the East Pacific Rise at 9°30′N, *J. Geophys. Res.*, *99*, 24,135–24,157.

White, R. S., and R. A. Stephen (1980), Compressional to shear wave conversion in oceanic crust, *Geophys. J.R. Astron. Soc.*, *63*, 547–565.

Woodward, M. (1992), Wave equation tomography, *Geophysics*, *57*, 15–26.

Wu, R.-S., and M. N. Töksoz (1987), Diffraction tomography and multisource holography applied to seismic imaging, *Geophysics*, *52*, 11–25.

Yilmaz, O. (2001), *Seismic Data Analysis*, vol. 1, *Processing, Inversion and Interpretation of Seismic Data*, Soc. of Explor. Geophys., Tulsa, Okla.

Zelt, C., and P. J. Barton (1998), Three-dimensional seismic refraction tomography: A comparison of two methods applied to data from the faeroe basin, *J. Geophys. Res.*, *103*(B4), 7187–7210.

Zelt, C., and R. B. Smith (1992), Seismic traveltime inversion for 2-d crustal velocity structure, *Geophys. J. Int.*, *108*, 16–34.

J.-X. Dessa and S. Operto, UMR Géosciences Azur-CNRS-IRD-UNSA-UPMC, BP 48 La Dares, F-06230 Villefranche-sur-mer, France. (dessa@geoazur.obs-vlfr.fr; operto@geoazur.obs-vlfr.fr)

J. Virieux, UMR Géosciences Azur-CNRS-IRD-UNSA-UPMC, 250, rue Albert Einstein, Sophia-Antipolis, F-06560, Valbonne, France. (viri@geoazur.unice.fr)